



Asteroseismology Sheds Light on the Origin of Carbon-deficient Red Giants: Likely Merger Products and Linked to the Li-rich Giants

Sunayana Maben^{1,2,3} , Simon W. Campbell^{4,5}, Yerra Bharat Kumar³, Bacham E. Reddy³, and Gang Zhao^{1,2} 

¹ CAS Key Laboratory of Optical Astronomy, National Astronomical Observatories, Chinese Academy of Sciences, Beijing 100101, Peoples Republic Of China
gzhao@nao.cas.cn

² School of Astronomy and Space Science, University of Chinese Academy of Sciences, Beijing 100049, Peoples Republic Of China

³ Indian Institute of Astrophysics, 2nd Block, Koramangala, Bangalore, 560034, India; bharat.yerra@iiap.res.in

⁴ School of Physics and Astronomy, Monash University, Clayton, Victoria, Australia

⁵ ARC Centre of Excellence for Astrophysics in Three Dimensions (ASTRO-3D), Australia

Received 2023 June 21; revised 2023 August 10; accepted 2023 August 10; published 2023 October 23

Abstract

Carbon-deficient red giants (CDGs) are a peculiar class of stars that have eluded explanation for decades. We aim to better characterize CDGs by using asteroseismology (Kepler, TESS) combined with spectroscopy (APOGEE, LAMOST), and astrometry (Gaia). We discovered 15 new CDGs in the Kepler field, and confirm that CDGs are rare, as they are only 0.15% of our background sample. Remarkably, we find that our CDGs are almost exclusively in the red clump (RC) phase. Asteroseismic masses reveal that our CDGs are primarily low-mass stars ($M \lesssim 2 M_{\odot}$), in contrast to previous studies, which suggested they are intermediate mass ($M = 2.5\text{--}5.0 M_{\odot}$) based on HR diagrams. A very high fraction of our CDGs (50%) are also Li-rich giants. We observe a bimodal distribution of luminosity in our CDGs, with one group having normal RC luminosity and the other being a factor of 2 more luminous than expected for their masses. We find demarcations in chemical patterns and luminosities, which lead us to split them into three groups: (i) normal-luminosity CDGs, (ii) overluminous CDGs, and (iii) overluminous highly polluted CDGs. We conclude that a merger of a helium white dwarf with a red giant branch star is the most likely scenario for the two groups of overluminous stars. Binary mass-transfer from intermediate-mass asymptotic giant branch stars is a possibility for the highly polluted overluminous group. For the normal-luminosity CDGs, we cannot distinguish between core He-flash pollution or lower-mass merger scenarios. Due to the overlap with the CDGs, Li-rich giants may have similar formation channels.

Unified Astronomy Thesaurus concepts: [Asteroseismology \(73\)](#); [Low mass stars \(2050\)](#); [Stellar abundances \(1577\)](#); [Chemically peculiar giant stars \(1201\)](#); [Stellar mergers \(2157\)](#)

Supporting material: machine-readable table


1. Introduction

When a star first ascends the red giant branch (RGB) the first dredge-up (FDU) occurs. In the FDU, the convective envelope moves inward (in mass) and mixes material from the interior to the surface. This material has been exposed to H-burning on the main sequence, and therefore the surface composition of the star changes. There is good agreement between theory (e.g., Iben 1964, 1967; Dearborn et al. 1976, 1978) and observation (e.g., Lambert & Ries 1977; Kjaergaard et al. 1982; Shetrone et al. 1993, 2019) on this event. The main surface abundance changes are an increase in the ^4He , ^{14}N , and ^{13}C abundances, and a decrease in the ^{12}C abundance by about 30% (Iben & Renzini 1984).

Contrary to this picture, 44 giants have been found to have extremely low carbon abundances (Bidelman 1951; Bidelman & MacConnell 1973; Bond 2019), well below what is expected from FDU. These stars are known as the weak *G*-band (wGb) stars, which are G and K giants whose spectra show very weak or absent *G*-band absorption of the CH molecule at 4300 Å. Of the 44 wGb stars, only 29 stars have carbon abundances from high-resolution spectra ($R \approx 48,000\text{--}60,000$; Adamczak & Lambert 2013; Palacios et al. 2016). When the high-resolution

spectra of these peculiar stars were analyzed in detail, in addition to these stars being extremely carbon-deficient, their carbon isotopic ratios $^{12}\text{C}/^{13}\text{C}$ were found to be close to the equilibrium value of 3–4. Also, N was found to be enhanced, and in some cases, they were found to be overabundant in Li and Na as well. These studies suggested that the wGb stars were probably intermediate-mass stars ranging in mass from about $2.5 M_{\odot}$ to $5.0 M_{\odot}$. Based on their position on the Hertzsprung–Russell diagram (HRD), many of them were shown to be in the subgiant branch (SGB)/RGB phase and a few in the core He-burning phase (red clump; RC). The first dedicated spectroscopic survey for C-deficient stars was undertaken 50 yr ago by Bidelman & MacConnell (1973). Recently, Bond (2019) added five carbon-deficient red giants (CDGs) based on spectroscopy to the initial list of CDGs. Finally, Maben et al. (2023) reported the identification of about 100 giants with medium to extreme carbon deficiency, based on the APOGEE survey⁶.

To this day, there is no consensus on why these giants have extremely low C and high N abundances. Some studies favor in situ origin, that is internal nucleosynthesis with extra-mixing in stars (Adamczak & Lambert 2013), and others favor an external origin such as pollution of their stellar atmospheres

 Original content from this work may be used under the terms of the [Creative Commons Attribution 4.0 licence](#). Any further distribution of this work must maintain attribution to the author(s) and the title of the work, journal citation and DOI.

⁶ We note that Maben et al. (2023) was published while the current study was in review.

during the main sequence (MS) or pre-main sequence (PMS) by CN-processed material (Palacios et al. 2016).

Two of the key factors that are required to decipher the possible origin of the carbon anomaly and its connection with other elements are the mass and evolutionary status of the wGb stars. Although there have been many attempts at determining these two stellar characteristics, the results so far have been inconclusive, since previous determinations have been based only on locations in the HRD (Palacios et al. 2012; Adamczak & Lambert 2013; Palacios et al. 2016; Bond 2019; Maben et al. 2023).

In the current study, we aim to determine the mass and evolutionary status of these peculiar stars. For the masses, we use asteroseismology combined with astrometry, photometry, and spectroscopy. For the evolutionary phase, we will use the period spacing of the g-dominated mixed modes (ΔP , $\Delta\Pi_1$) to determine if the wGb stars are in the RGB phase or He-core burning RC phase (Bedding et al. 2011; Mosser et al. 2014). These results, combined with chemical composition information, will hopefully allow us to better understand the origin of the carbon (and other) anomalies in these stars.

To this end, in Section 2 we build a catalog by conducting a large systematic search of wGb stars that have both asteroseismic data from the Kepler mission (Borucki et al. 2010), and spectroscopic data from the Apache Point Observatory Galactic Evolution Experiment (APOGEE) survey (Majewski et al. 2017). The results are presented in Section 3. We provide substantial discussion on the implications of our results in Section 4, and our conclusions are summarized in Section 5.

2. Sample Selection

2.1. APOGEE-KEPLER Crossmatch

We take the spectroscopic data from data release 17 (DR17; Abdurro'uf et al. 2022) of APOGEE, which is a large-scale near-IR, high-resolution ($R \approx 22,500$) survey. Stellar parameters and individual elemental abundances for up to 20 species were derived by the APOGEE Stellar Parameters and Chemical Abundances Pipeline (ASPCAP; García Pérez et al. 2016) for 733,901 stars across the Milky Way.

In the current study, we focus on the Kepler field since we are interested in having asteroseismic constraints. We use the Kepler stellar properties catalog by Mathur et al. (2017). This catalog is based on Kepler data release 25, which contains data from Quarters 1–17. It is the largest catalog of stars observed by the Kepler mission with 197,096 individual targets.

To begin with, we crossmatched these two catalogs, which yielded a sample of 23,129 stars (APOGEE-KEPLER sample). Second, we checked how many of these stars have global asteroseismic parameters derived from precision Kepler light curves in the literature (Stello et al. 2013; Mosser et al. 2014; Vrad et al. 2016; Serenelli et al. 2017; Pinsonneault et al. 2018; Yu et al. 2018; Li et al. 2020). We found 11,099 stars (i.e., 48% of the APOGEE-KEPLER sample) that matched this criterion.

Further, we constrain our sample to have good-quality APOGEE spectroscopic data. The ASPCAPFLAG is used to flag potential issues with an observation and/or with specific stellar parameters. Hence, we remove stars with flags STAR_BAD or STAR_WARN. Since we also require reliable metallicity and carbon abundances, we limit our sample to stars

that have FE_H_FLAG=0 and C_FE_FLAG=0 (Jönsson et al. 2020).

We restrict our sample to disk metallicities ($[\text{Fe}/\text{H}] \geq -0.8$ dex; Tomkin et al. 1995). This is consistent with the known wGb stars. Carbon is more complex at low metallicities since there is a significant dispersion in abundances (e.g., Romano et al. 2019). In addition, there is a known carbon-depletion mechanism—deep-mixing in red giants—that increases the carbon depletion rate at low metallicities (e.g., Martell et al. 2008; Gerber et al. 2019). These constraints give us 10,674 stars (i.e., 46% of the APOGEE-KEPLER sample).

One of the primary purposes of this study is to determine the evolutionary phase of CDGs. We therefore select stars that have their evolutionary status positively determined in the different asteroseismic studies mentioned above. Applying this criterion, we obtain a final common sample of 10,180 stars (i.e., 44% of the APOGEE-KEPLER sample).

2.2. Defining and Identifying Carbon-deficient Stars

Figure 1 shows the APOGEE-KEPLER common sample that made it through the quality criteria discussed in Section 2.1. In the left panel of the figure, we see that we have a sample that covers all of the evolutionary phases, from dwarfs and subgiants to H-shell burning stars and core He-burning (CHeB) stars. The distribution of the carbon abundance for the sample is shown in the central panel. It can immediately be seen that there are very few outliers, with low $[\text{C}/\text{Fe}]$.

Here we want to make a quantitative definition of carbon-deficient stars. To guide us, we use stellar models, which illustrate the theoretical expectations for the carbon surface abundances. We calculated a series of models using the MESA stellar code (Paxton et al. 2011, 2019; version 12778). RGB mass loss was modeled using the Reimers (1975) formula ($\eta = 0.3$). We used the standard MESA nuclear network (“basic.net”), standard equation of state (see Paxton et al. 2019 for details), and $\alpha_{\text{MLT}} = 2.0$. Convective boundary locations were based on the Schwarzschild criterion, extended with exponential overshoot (Herwig et al. 1997) during core helium burning ($f_{\text{OS}} = 0.001$; following Constantino et al. 2017). Models were run from the PMS to the start of the thermally pulsing-asymptotic giant branch (TP-AGB) phase, so as to cover the CHeB phase for which we have many stars in our sample. In Figure 1 we show two of our models, having masses of $1 M_{\odot}$ and $2 M_{\odot}$. These model masses are representative of the bulk of the background observational sample. There is a metallicity distribution in our sample with $[\text{Fe}/\text{H}]$ ranging from -0.8 to $+0.5$ dex and peaking at $[\text{Fe}/\text{H}] = 0.0$ dex. Our models showed that metallicity has a much smaller effect than mass on $[\text{C}/\text{Fe}]$, so we only show $[\text{Fe}/\text{H}] = 0.0$ models for clarity. As can be seen in Figure 1, the models start at $[\text{C}/\text{Fe}] = 0.0$ then deplete C around $\log(g) = 3.2$ – 3.5 , as the convective envelope deepens during FDU early on the RGB. By $\log(g) \approx 2.8$ – 3.2 , the surface C abundances have reached their minima, with a total $[\text{C}/\text{Fe}]$ reduction of 0.05 dex and 0.18 dex for the $1 M_{\odot}$ and $2 M_{\odot}$ models, respectively. From then on, the C remains constant.

The initial C abundance of a star will affect its future surface abundance. Our sample includes dwarf stars that have abundances as low as $[\text{C}/\text{Fe}] \simeq -0.15$ dex. To roughly account for stars with lower initial C, we offset the $2 M_{\odot}$ model track (which has the largest C depletion) by -0.15 dex (similar to Mishenina et al. 2006 and Tautvaišienė et al. 2010). Here, the

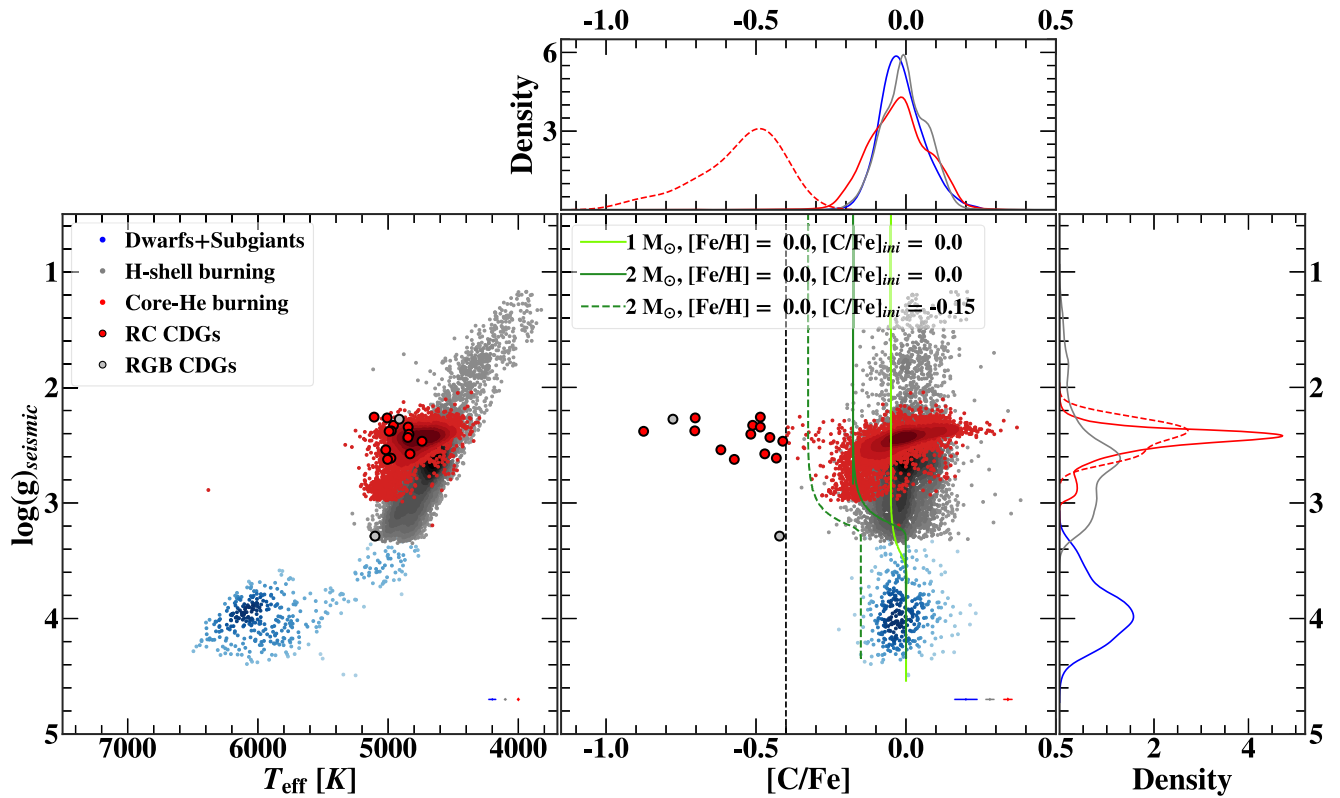


Figure 1. Hertzsprung–Russell diagram (left) and $\log(g)_{\text{seis}}$ as a function of $[C/Fe]$ (right). Our APOGEE-KEPLER common sample forms the background in a color scale that represents the number density of stars; darker colors indicate higher density. Dwarfs and subgiants (blue dots), inert He-core giants ascending the RGB for the first time (gray dots), and He-core burning giants (red dots) are shown. Kernel density histograms are included to show the $\log(g)$ and $[C/Fe]$ distributions for various parts of the sample, with the color scheme following the background sample, and the dashed histogram showing our final C-deficient sample. We superimpose model tracks in the $\log(g)$ - $[C/Fe]$ plane for comparison (see the text for model details). Starting with an initial $[C/Fe]_{\text{ini}} = 0.0$, the models show a reduction of $[C/Fe]$ by ≈ 0.05 – 0.2 dex, due to FDU dilution. As some dwarf stars have lower $[C/Fe]$, which may reflect a lower initial abundance, we offset the $2 M_{\odot}$ model (which has the larger C-depletion) by -0.15 dex to match the lower envelope of those stars. This indicates the expected lower limit of $[C/Fe]$ for later phases of evolution (dashed model line). The vertical dashed line at $[C/Fe] = -0.4$ dex denotes the cut we use to define carbon-deficient stars (see the text for details). The larger symbols (filled circles) show our carbon-deficient sample. Large red circles are RC stars, and the two large gray circles are RGB stars. Formal error bars are shown on the bottom-right end of each subplot. The top and right panels of the right subplot show kernel density histograms for the normal giants (solid lines) and RC CDGs (dashed red line). We use the solar abundance of C as derived by Grevesse et al. (2007).

carbon depletion reaches as low as $[C/Fe] \simeq -0.33$ dex. Based on this, and the observed distribution of the low-carbon tail, we make a conservative cut at $[C/Fe] = -0.4$ dex, below which we consider all stars as carbon-deficient (vertical dashed line in Figure 1). With this definition, we find a total of 15 carbon-deficient stars, 0.15% of our final APOGEE-KEPLER sample. This highlights how rare carbon-deficient stars are. We will be referring to these stars as the “CDGs.” All stars in our CDG sample have known evolutionary phases. In Figure 1, we indicate their respective evolutionary phases using different symbols. Thirteen of our CDGs are RC stars, and two are RGB stars (although we later re-classify one of those as RC; see Section 3.2).

3. Analysis and Results

3.1. Evolutionary Phase: Seismic Diagram

It has been shown that RC and RGB stars can be separated by considering measurements of their mixed-mode period spacing ΔP (Bedding et al. 2011) or equivalently, the asymptotic g-mode period spacing $\Delta\Pi_1$ (Mosser et al. 2014). Red giants with $\Delta\Pi_1 \geq 80$ s are RC stars, and the giants in the very narrow strip (Figure 2) with $\Delta\Pi_1 \leq 80$ s are RGB stars (Vrard et al. 2016).

Out of our 15 CDGs, six stars have both the asteroseismic parameters $\Delta\Pi_1$ and $\Delta\nu$ from Mosser et al. (2014), and five stars have these parameters from Vrard et al. (2016).⁷ In Figure 2 we plot these 11 RC stars (large symbols) over the background sample of Mosser et al. (2014). We have limited the background sample to match our RC sample mass range of $1.0 M_{\odot} \leq M \leq 2.5 M_{\odot}$ (Section 3.2.1) for better comparison.

As seen in Figure 2, all of our CDGs with $\Delta\Pi_1$ have large values of this parameter. They also have small values of $\Delta\nu$ ($< 5 \mu\text{Hz}$). They clearly occupy the He-core burning phase region of the $\Delta\Pi_1$ - $\Delta\nu$ diagram. Two of the CDGs are classified as Helium subflashing stars by Mosser et al. (2014; see discussion in Section 4.4.1).

3.2. Luminosities

Luminosities of the CDGs were determined using the standard formula.⁸ Distances were taken from the catalog of Bailer-Jones et al. (2021). The visual magnitudes and their errors were estimated from the color–color transformations given in Riello et al. (2021) that relate the Gaia DR3 photometric system to the Johnson-Cousins system (Stetson 2000). We used the

⁷ The single RGB star (see Section 3.2) does not have a reported $\Delta\Pi_1$, but it is clearly of too low luminosity to be an RC star.

⁸ $\log(L/L_{\odot}) = -0.4 [V_0 - (m - M)_0 + BC - M_{\text{bol},\odot}]$.

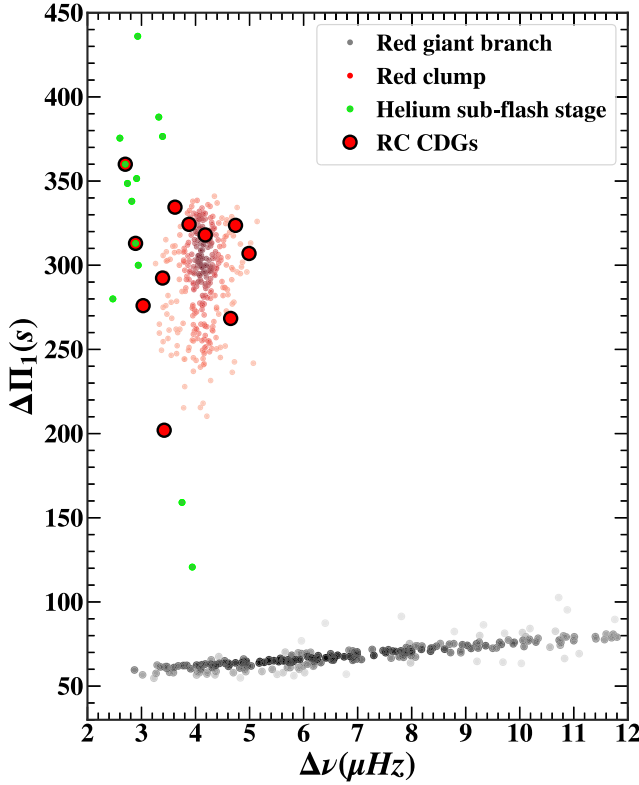


Figure 2. Seismic diagram of our RC CDGs, which have known $\Delta\Pi_1$ and $\Delta\nu$ (11 stars; large filled red circles). Giants classified based on asteroseismic analysis from the background from Mosser et al. (2014; small filled circles; see key), in a color scale that represents the number density of stars; darker colors indicate higher densities.

Green et al. (2019) three-dimensional dust map to estimate the reddening for each of the stars. We applied bolometric corrections following Alonso et al. (1999), adopting errors in T_{eff} and $[\text{Fe}/\text{H}]$ of 50 K and 0.05 dex, respectively. Our derived luminosities are listed in Table 1.

All of our stars, except one (KIC 8352953), have luminosities consistent with being RC stars (Table 1; see also the Kiel diagram in Figure 1). KIC 8352953 has a luminosity that coincides with the lower-RGB phase and is classified as an RGB star in Yu et al. (2018). All except one of the stars (KIC 8222189) that have RC luminosities are classified as RC stars by asteroseismic studies (Stello et al. 2013; Mosser et al. 2014; Vrad et al. 2016; Pinsonneault et al. 2018; Yu et al. 2018). This one star has a stellar evolutionary phase of RGB (or AGB) in Pinsonneault et al. (2018), is unclassified in Yu et al. (2018) and Elsworth et al. (2017), but is classified as a RC star by Ting et al. (2018). Given that KIC 8222189 has a luminosity and surface gravity that are consistent with the core He-burning phase, we classify it as an RC star from now on, but note that a ΔP measurement would be required to be certain. In summary, our CDG sample has one RGB star and 14 RC stars.

Looking at the distribution of the luminosities, we find there is a bimodality (see Figure 3), with one group having higher luminosity ($\log(L/L_{\odot}) = 2.1 \pm 0.1$ dex) than the other ($\log(L/L_{\odot}) = 1.8 \pm 0.1$ dex). Interestingly the brighter RC stars tend to have the lowest C abundances (see Figures 3 and 4). The bimodality is also present in $\log(g)$ but is not as clear (Figure 1). We discuss this bimodality in detail in Section 3.6.

3.2.1. Masses

The masses of the CDGs were determined using several combinations of the seismic (ν_{max} , $\Delta\nu$) and nonseismic parameters (T_{eff} , L/L_{\odot} , g) that were available. The global seismic parameters are correlated with fundamental stellar properties; $\nu_{\text{max}} \propto gT_{\text{eff}}^{-1/2}$ and $\Delta\nu \propto \rho^{-1/2}$, where g is the surface gravity, and ρ is the mean density of the star (Ulrich 1986; Brown et al. 1991; Kjeldsen & Bedding 1995). Combining these relations with the Stefan–Boltzmann luminosity law, $L \propto R^2 T_{\text{eff}}^4$, allows the derivation of the four seismic mass equations (Equations (1)–(4); e.g., Miglio et al. 2016; Howell et al. 2022). Equation (5) is a standard, but nonseismic mass formula, which uses the photometric and spectroscopic parameters of a star. We determined the masses of the CDGs using all five of these mass equations:

$$\left(\frac{M}{M_{\odot}}\right) \simeq \left(\frac{\nu_{\text{max}}}{\nu_{\text{max},\odot}}\right)^3 \left(\frac{\Delta\nu}{\Delta\nu_{\odot}}\right)^{-4} \left(\frac{T_{\text{eff}}}{T_{\text{eff},\odot}}\right)^{3/2} \quad (1)$$

$$\left(\frac{M}{M_{\odot}}\right) \simeq \left(\frac{\Delta\nu}{\Delta\nu_{\odot}}\right)^2 \left(\frac{L}{L_{\odot}}\right)^{3/2} \left(\frac{T_{\text{eff}}}{T_{\text{eff},\odot}}\right)^{-6} \quad (2)$$

$$\left(\frac{M}{M_{\odot}}\right) \simeq \left(\frac{\nu_{\text{max}}}{\nu_{\text{max},\odot}}\right) \left(\frac{L}{L_{\odot}}\right) \left(\frac{T_{\text{eff}}}{T_{\text{eff},\odot}}\right)^{-7/2} \quad (3)$$

$$\left(\frac{M}{M_{\odot}}\right) \simeq \left(\frac{\nu_{\text{max}}}{\nu_{\text{max},\odot}}\right)^{12/5} \left(\frac{\Delta\nu}{\Delta\nu_{\odot}}\right)^{-14/5} \left(\frac{L}{L_{\odot}}\right)^{3/10} \quad (4)$$

$$\left(\frac{M}{M_{\odot}}\right) \simeq \left(\frac{L}{L_{\odot}}\right) \left(\frac{g}{g_{\odot}}\right) \left(\frac{T_{\text{eff}}}{T_{\text{eff},\odot}}\right)^{-4}. \quad (5)$$

Here, we use $\nu_{\text{max},\odot} = 3090 \pm 30 \mu\text{Hz}$, $\Delta\nu_{\odot} = 135.1 \pm 0.1 \mu\text{Hz}$ (both from Huber et al. 2011), $T_{\text{eff},\odot} = 5777$ K, and $\log(g)_{\odot} = 4.44$ (both from Morel et al. 2014) as our adopted solar values.

For Equations (1), (2), and (4), it is known that one needs to apply a correction to the observed $\Delta\nu$ for use in the scaling relations (e.g., White et al. 2011; Miglio 2012). We calculate $\Delta\nu$ corrections using ASFGGRID (Sharma et al. 2016) and apply these to the $\Delta\nu$ values of the CDGs obtained from Mosser et al. (2014) and Vrad et al. (2016) only, as Yu et al. (2018) provides corrected $\Delta\nu$.

We list our mass determinations for all 15 CDGs using each of the five mass equations in Table 1. We also show them graphically in Figure 5, where we compare the individual masses of the RC CDG stars calculated with each equation.

As a summary, we show in Table 2 the average uncertainties on the masses for each equation, along with the average masses for each equation. It can be seen that the masses calculated with asteroseismic Equation (2) have the largest uncertainties $\overline{\sigma}/\overline{M} = 1.26 M_{\odot}$; also see error bars in Figure 5), when compared to the uncertainties from asteroseismic Equations (1), (3), and (4), which all have similar uncertainties ($0.14 M_{\odot}$ – $0.17 M_{\odot}$). The nonseismic Equation (5) has larger uncertainties ($0.27 M_{\odot}$) than the asteroseismic equations (apart from Equation (2)), but is still of the same order of magnitude as the more accurate seismic equations. From now on, we do not use the Equation (2) masses, due to the large uncertainties.

For our final seismic masses, we take an average of the three remaining seismic mass equations for each individual star (M_{avg} in Table 1). In Figure 6 we show these masses versus the nonseismic mass determinations. The seismic mass range of

Table 1
Atmospheric, Asteroseismic, Kinematic Parameters Along with the CNO Abundance Ratios and Mass Estimates from Equations (1)–(5) of the CDGs

KIC	T_{eff} (K)	[Fe/H]	$\log(g)_{\text{seis}}^c$ (cm s^{-2})	$\log(L/L_{\odot})$	ν_{max}^c (μHz)	$\Delta\nu$ (μHz)	$\Delta\Pi_1$ (s)	[C/Fe]	[N/Fe]	[O/Fe]	M_1 (M_{\odot})	M_2 (M_{\odot})	M_3 (M_{\odot})	M_4 (M_{\odot})	M_{avg} (M_{\odot})	M_5 (M_{\odot})	R_{seis} (R_{\odot})	b (deg)	Z (kpc)
5881715	4840	-0.12	2.41 ± 0.02	1.89 ± 0.05	30.90	3.42^a	202^a	-0.52	0.53	-0.02	1.91 ± 0.22	1.26 ± 1.86	1.44 ± 0.18	1.76 ± 0.17	1.70	1.35 ± 0.23	14.46 ± 0.63	10.15	0.33
8879518	4832	0.08	2.58 ± 0.01	1.73 ± 0.04	46.18	4.65^b	268^b	-0.47	0.61	-0.01	1.87 ± 0.14	1.35 ± 2.12	1.50 ± 0.15	1.74 ± 0.11	1.70	2.11 ± 0.32	11.66 ± 0.35	14.46	0.32
4071012	4992	0.07	2.38 ± 0.01	2.07 ± 0.04	29.20	3.03^b	276^b	-0.87	0.68	-0.11	2.74 ± 0.25	1.53 ± 0.84	1.85 ± 0.19	2.43 ± 0.18	2.34	2.81 ± 0.43	17.65 ± 0.70	8.18	0.27
3355015	4846	-0.15	2.34 ± 0.02	1.81 ± 0.05	26.98	3.39^a	292^a	-0.49	0.57	0.03	1.31 ± 0.14	0.94 ± 1.31	1.04 ± 0.13	1.22 ± 0.11	1.19	1.06 ± 0.18	12.76 ± 0.51	8.15	0.29
3736289	4978	-0.10	2.61 ± 0.01	1.80 ± 0.04	49.94	4.99^a	307^a	-0.43	0.52	-0.04	1.87 ± 0.17	1.65 ± 0.98	1.72 ± 0.18	1.82 ± 0.14	1.80	1.60 ± 0.24	11.16 ± 0.37	12.78	0.28
5446927	5107	-0.74	2.26 ± 0.01	2.05 ± 0.05	21.88	2.89^a	313^a	-0.49	0.47	0.15	1.46 ± 0.12	1.12 ± 0.39	1.22 ± 0.15	1.38 ± 0.10	1.36	1.34 ± 0.22	14.80 ± 0.51	11.36	0.50
4667911	4740	0.08	2.47 ± 0.01	1.67 ± 0.04	36.37	4.18^b	318^b	-0.41	0.53	-0.03	1.34 ± 0.13	1.00 ± 3.43	1.10 ± 0.11	1.26 ± 0.10	1.23	0.98 ± 0.15	11.19 ± 0.42	8.34	0.15
5000307	5018	-0.29	2.54 ± 0.01	1.75 ± 0.04	42.16	4.74^a	324^a	-0.62	0.63	-0.01	1.39 ± 0.09	1.20 ± 0.57	1.26 ± 0.13	1.35 ± 0.07	1.33	1.49 ± 0.23	10.43 ± 0.26	13.20	0.33
11971123	4848	-0.13	2.43 ± 0.01	1.79 ± 0.04	32.47	3.88^b	324^b	-0.45	0.52	0.05	1.33 ± 0.13	1.14 ± 1.58	1.20 ± 0.12	1.29 ± 0.10	1.27	1.37 ± 0.21	11.74 ± 0.45	13.04	0.31
8110538	4975	-0.59	2.38 ± 0.02	1.98 ± 0.05	28.77	3.62^b	334^b	-0.70	0.80	0.49	1.29 ± 0.14	1.62 ± 1.00	1.50 ± 0.19	1.35 ± 0.12	1.38	1.12 ± 0.19	12.19 ± 0.52	9.74	0.62
2423824	5007	-0.39	2.26 ± 0.01	2.15 ± 0.05	22.02	2.70^a	360^a	-0.70	0.63	0.08	1.88 ± 0.18	1.56 ± 0.81	1.66 ± 0.20	1.81 ± 0.14	1.79	1.71 ± 0.29	16.85 ± 0.67	13.59	0.49
8352953	5101	-0.18	3.29 ± 0.01	1.10 ± 0.04	230.27	16.74^c		-0.42	0.63	0.24	1.46 ± 0.07	1.45 ± 0.48	1.45 ± 0.15	1.46 ± 0.07	1.45	1.66 ± 0.25	4.56 ± 0.08	16.27	0.26
7848354	5004	-0.08	2.62 ± 0.02	1.75 ± 0.06	51.74	4.67^c		-0.57	0.59	0.03	2.66 ± 0.26	1.19 ± 0.64	1.56 ± 0.23	2.26 ± 0.20	2.16	1.67 ± 0.31	13.05 ± 0.44	7.59	0.42
4830861	4959	-0.12	2.33 ± 0.01	2.14 ± 0.05	25.94	2.96^c		-0.51	0.56	0.01	2.06 ± 0.18	1.94 ± 1.29	1.98 ± 0.24	2.03 ± 0.15	2.02	2.67 ± 0.45	16.26 ± 0.59	11.81	0.43
8222189	4914	-0.09	2.28 ± 0.02	2.17 ± 0.04	23.02	2.69^c		-0.78	0.65	-0.06	2.07 ± 0.38	1.88 ± 1.62	1.94 ± 0.22	2.03 ± 0.30	2.02	2.43 ± 0.37	17.37 ± 1.16	15.57	0.35

Notes. We have adopted the errors in T_{eff} and [Fe/H] as 50 K and 0.05 dex, respectively, for all of the stars. M_{avg} is the average of the asteroseismic mass Equations (1), (3), and (4).

^a Mosser et al. (2014).

^b Vrad et al. (2016).

^c Yu et al. (2018).

(This table is available in its entirety in machine-readable form.)

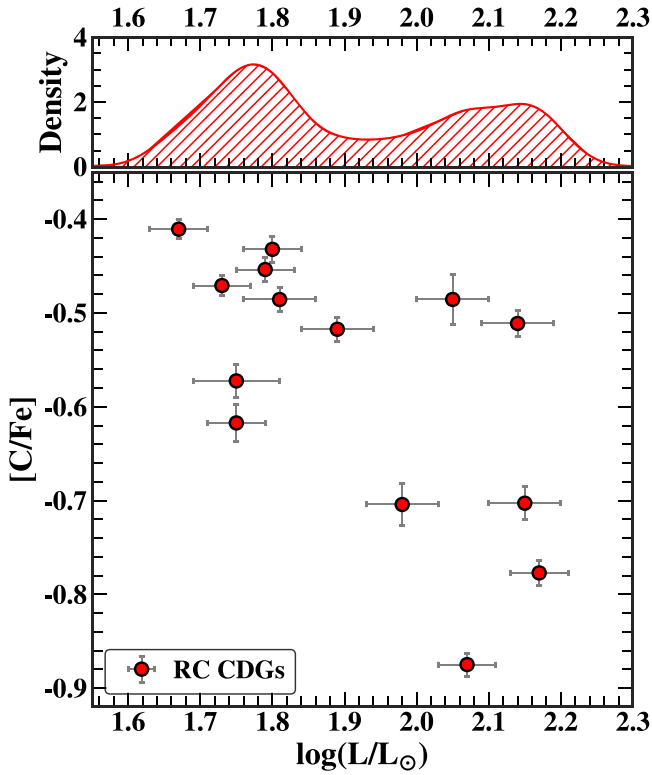


Figure 3. Carbon abundance as a function of $\log(L/L_{\odot})$ for our RC CDGs. As can be seen in the Gaussian kernel density histogram above, the luminosity distribution is bimodal. This bimodality is discussed in detail in Section 3.6. We use the solar abundance of C as derived by Grevesse et al. (2007).

our RC CDGs is $1.2 M_{\odot} \leq M \leq 2.3 M_{\odot}$ (with average standard deviation between mass equations of $0.2 M_{\odot}$). The nonseismic mass equation gives a slightly expanded mass range of $1.0 M_{\odot} \leq M \leq 2.8 M_{\odot}$, with slightly higher average uncertainties ($0.3 M_{\odot}$).

For the single RGB star, the seismic mass is $1.5 \pm 0.1 M_{\odot}$, and the nonseismic mass is $1.7 \pm 0.3 M_{\odot}$.

3.3. Radius Determination

We calculated the seismic stellar radius for our CDGs using the equation (Ulrich 1986; Kjeldsen & Bedding 1995):

$$\left(\frac{R}{R_{\odot}}\right) \simeq \left(\frac{\nu_{\max}}{\nu_{\max,\odot}}\right) \left(\frac{\Delta\nu}{\Delta\nu_{\odot}}\right)^{-2} \left(\frac{T_{\text{eff}}}{T_{\text{eff},\odot}}\right)^{1/2}. \quad (6)$$

We have used corrected $\Delta\nu$ values of the CDGs, along with the ν_{\max} and T_{eff} values as stated in Table 1. The seismic radii estimates for all 15 CDGs are also provided in Table 1.

We compare the seismic radius to independent radius estimates calculated using the Stefan–Boltzmann law in Figure 6. While having greater average uncertainties ($\simeq 0.8 R_{\odot}$) than the asteroseismic equation ($\simeq 0.5 R_{\odot}$), the nonseismic radius equation is nonetheless of the same order of magnitude as the more precise seismic equation. Between these two methods, all of the RC CDG radii, except two, agree within the 2σ uncertainties.

The seismic radius range of all of the RC CDGs is about $10\text{--}18 R_{\odot}$. Ignoring the two outliers, there is a slight offset between the seismic and nonseismic radii estimates of $\simeq 0.5 R_{\odot}$, where the seismic radii are larger.

For the RGB star, the seismic radius ($4.6 \pm 0.1 R_{\odot}$) and the nonseismic radius ($4.6 \pm 0.3 R_{\odot}$) agree with each other perfectly.

3.4. Kinematics

Here we compile the kinematic properties of our sample of CDGs and determine what component(s) of the Galaxy they belong to.

We calculated the Galactic space velocity components (U , V , W) for each star using astrometry with distances taken from the catalog of Bailer-Jones et al. (2021) and proper motions from Gaia DR3 (Gaia Collaboration et al. 2016, 2022). The radial-velocity data was taken from APOGEE DR17. We have adopted the Sun’s distance from the Galactic center as 8.2 kpc (Bland-Hawthorn & Gerhard 2016), and its distance above the Galactic plane as 25 pc (Jurić & Ivezić 2008). The space velocity components were computed using the Astropy Galactocentric package (Astropy Collaboration et al. 2013, 2018). Space velocities are converted to the local standard of rest (LSR) frame using the solar motion (U_{\odot} , V_{\odot} , W_{\odot}) = (11.1, 12.24, 7.25) km s^{-1} (Bland-Hawthorn & Gerhard 2016). We adopt an LSR velocity $V_{\text{LSR}} = 232.8 \text{ km s}^{-1}$.

In Figure 7, our CDG sample is plotted in the Toomre diagram. We apply limits from Nissen (2004; also Venn et al. 2004) that define the different Galactic components. We find our CDGs are distributed in all components of the Galaxy—the thin disk, thick disk, and one star in the halo.

3.5. Abundances

3.5.1. Carbon, Nitrogen, and Oxygen

In Figure 8 we plot the C, N, and O abundances, the $[\text{C+N/Fe}]$ and $[\text{C+N+O/Fe}]$ sums, and the $[\text{C/N}]$ ratio against $[\text{Fe/H}]$ for a background sample of RC stars (Vrard et al. 2016), along with our CDG stars. All abundances are from the APOGEE catalog (DR17; García Pérez et al. 2016; Abdurro’uf & Aerts 2022). All stars have good-quality abundances ($X_{\text{FE_FLAG}}=0$; Jönsson et al. 2020). The background sample has been limited in mass $1.0 M_{\odot} \leq M \leq 2.5 M_{\odot}$, to match the mass range of our RC CDGs (Section 3.2.1).

The nitrogen abundances of the CDGs are enhanced by an average of $+0.35$ dex over the average $[\text{N/Fe}]$ of the background RC sample. This is a smaller offset than for $[\text{C/Fe}]$ (-0.52 dex). Due to the C and N offsets being in different directions, the average $[\text{C/N}]$ offset is large, at $+0.86$ dex. In contrast, the $[\text{O/Fe}]$ values of the CDGs generally track the abundances of the background sample. Most are close to scaled solar, except for three stars, which have higher $[\text{O/Fe}]$. Two of these stars are our most metal-poor objects. Looking at Mg (Figure 8), it shows the same pattern as oxygen, so we suggest that these three stars were likely α -enhanced from birth.

When we sum C and N, we see that most of the stars are scaled solar. The exceptions are the three α -enhanced stars. This again suggests that these three stars had different (non-scaled-solar) initial abundances. This is even more evident in the $[\text{C+N+O/Fe}]$ plot.

The strong N overabundance anticorrelated with the C under-abundance, along with the $[\text{C+N+O/Fe}]$ sum being mostly scaled solar, indicates that the material in the atmospheres of CDGs has been processed through CNO cycle hydrogen burning. We see no evidence for O depletion, and therefore infer that the ON cycle was not operating significantly, i.e., only CN cycling occurred.

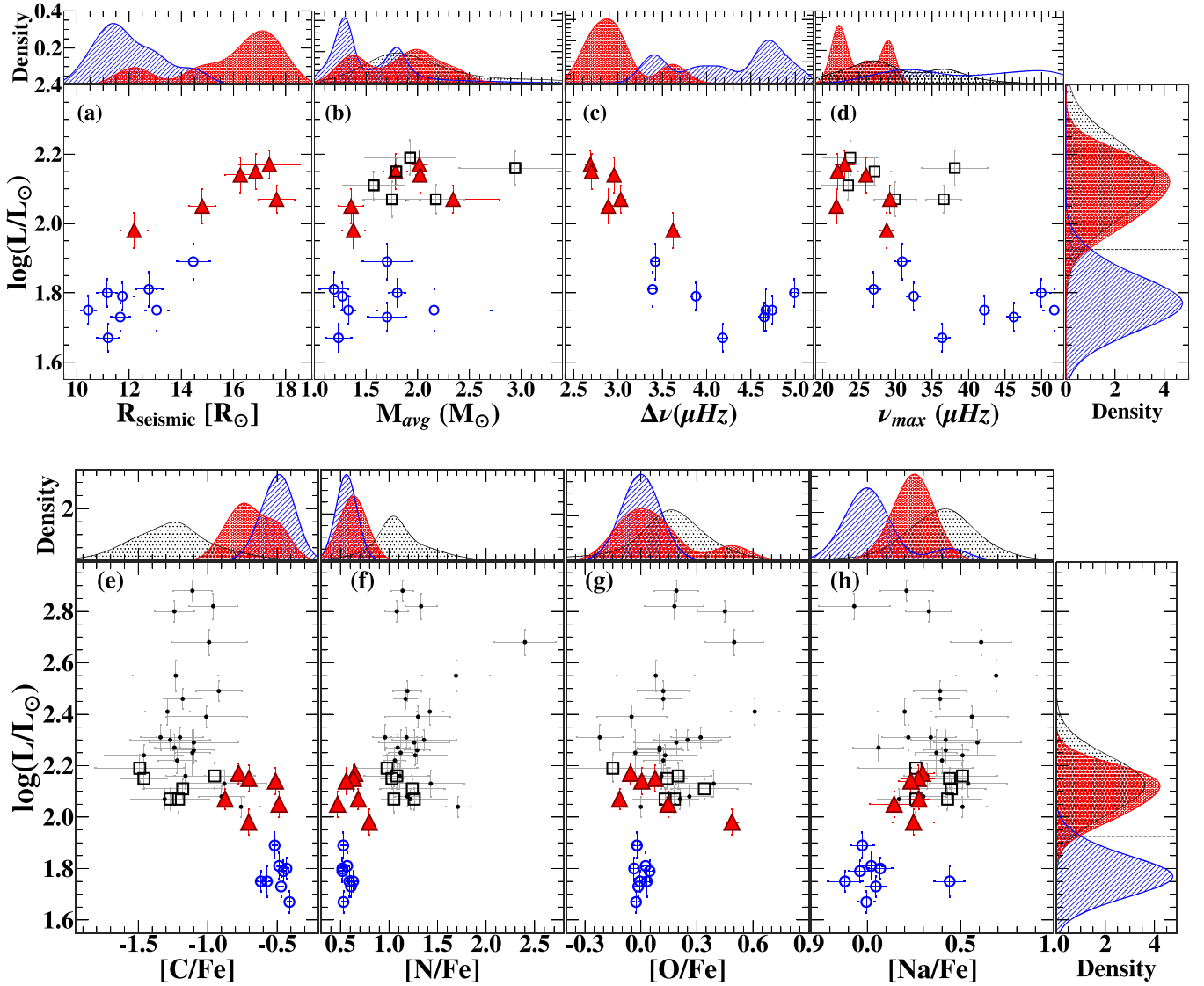


Figure 4. Top panel: $\log(L/L_{\odot})$ as a function of asteroseismic radius, mass, $\Delta\nu$, and ν_{\max} . Bottom panel: $\log(L/L_{\odot})$ as a function of the carbon, nitrogen, oxygen, and sodium abundances. Kernel density histograms are included to show the distributions for the RC CDGs, with the color scheme following the sample. The horizontal dashed line at $\log(L/L_{\odot}) = 1.925$ dex, denotes the cut we use to define two different luminosity groups of our RC CDG sample (see the text for details). The large filled red triangles and open blue circles show our overluminous-RC CDGs and normal-luminosity-RC CDGs, respectively. Large black squares are the known wGb stars that have asteroseismic parameters from Hon et al. (2021) and the small black circles are the rest of the known wGb stars from the literature. The abundances of the known wGb stars are from high-resolution optical spectra (Adamczak & Lambert 2013; Palacios et al. 2016). In order to compare the abundances of the known wGb with those of our CDG sample, they need to be on the same scale. We apply average offsets of $+0.02$, -0.15 , -0.12 , -0.11 , and -0.03 dex to the $[C/Fe]$, $[N/Fe]$, $[O/Fe]$, $[Na/Fe]$, and $[Fe/H]$ values of known wGb, respectively, to account for the systematic difference between the abundances from IR and optical spectra (Jönsson et al. 2020). The top and right panels of all of the subplots show kernel density histograms for the RC CDGs (dashed blue lines and large red dots) and known wGb stars with asteroseismic parameters (small black dots). We use the solar abundance of C, N, O, and Na as derived by Grevesse et al. (2007).

Since AGB stars increase $[C+N+O/Fe]$ through third dredge-up (e.g., Karakas & Lattanzio 2014), they are unlikely to be polluters for our sample. More generally, any scenario in which He-burning products are mixed into the polluting material is not supported by our observations. This is discussed further in Section 4.2.

3.5.2. Sodium, Magnesium, and Aluminum

The Na, Mg, and Al abundances versus metallicity of our CDG stars are shown in Figure 8, against a background sample of RC stars from Vrad et al. (2016).

Interestingly, Figure 8 shows that the sample splits into two groups in $[Na/Fe]$, one with enhanced $[Na/Fe]$ and one with scaled-solar Na. Taking a cut in $[Na/Fe]$ at $\sim +0.10$ dex, for the Na-enhanced group, we find an average sodium abundance

of $[Na/Fe] = 0.3 \pm 0.1$ dex, and the Na-normal group has $[Na/Fe] = 0.0 \pm 0.1$ dex. We discuss the implications of this Na bimodality (and its correlation with the luminosity bimodality; Section 3.6) in Section 4.

The $[Mg/Fe]$ and $[Al/Fe]$ abundances of the CDGs are consistent with those of the background sample. As mentioned, the three stars that appeared to be α -enhanced in the $[O/Fe]$ - $[Fe/H]$ plane of Figure 8 are those enhanced with the α -element Mg as well. Thus, it is likely that these three stars had different (non-scaled-solar) initial abundances, as suggested in Section 3.5.1.

3.5.3. Lithium

We crossmatched our CDG sample with the LAMOST survey (Zhao et al. 2006, 2012), which contains the 6707.8 Å Li line. We found 11 out of the 15 CDGs to have low-resolution spectra

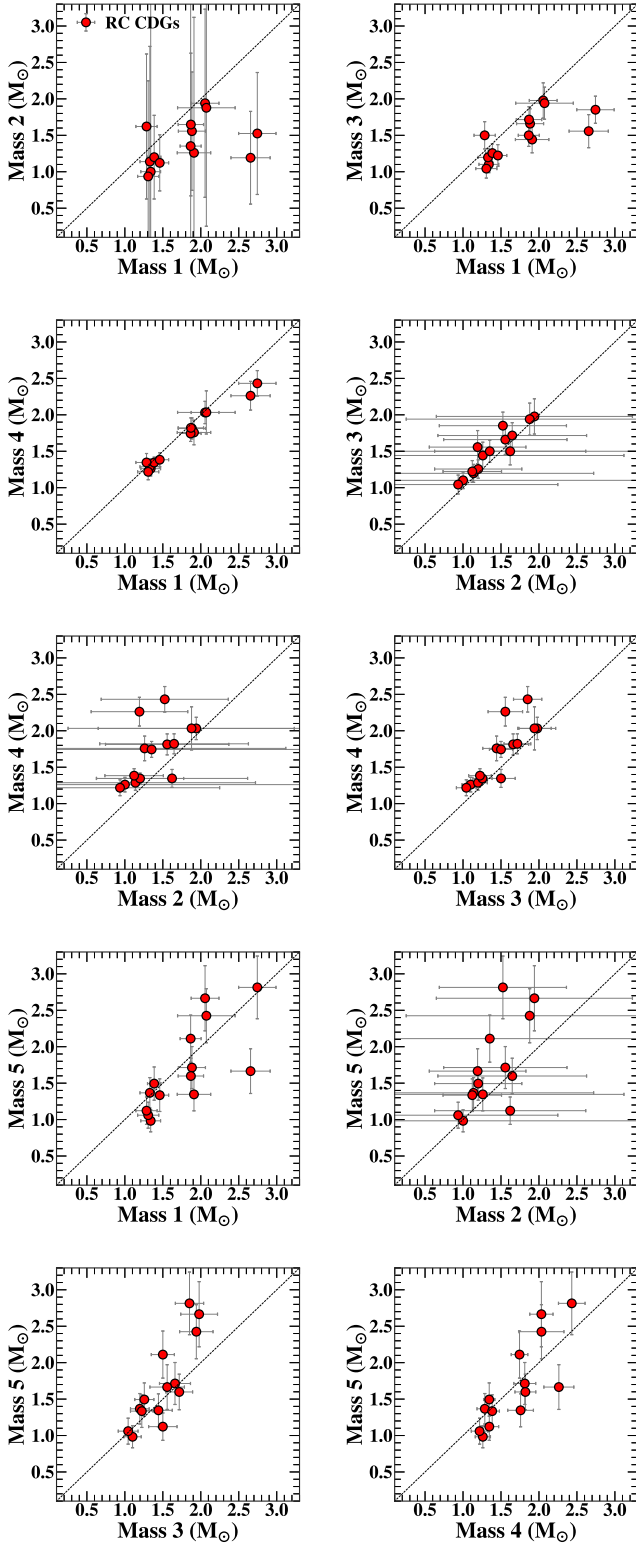


Figure 5. Comparison of various mass estimates of the RC CDGs using Equations (1)–(5).

($R \approx 1800$; see top panel of Figure 9). Only one star had a medium-resolution spectrum ($R \approx 7500$; see bottom panel of Figure 9). This star (KIC 8879518) has been previously identified to be a super-Li-rich star with $A(\text{Li})^9 = 3.51 \pm 0.12$ dex using this spectrum (Singh et al. 2021).

⁹ $A(\text{Li}) = \log(n(\text{Li})/n(\text{H})) + 12$, where n is the number density of atoms.

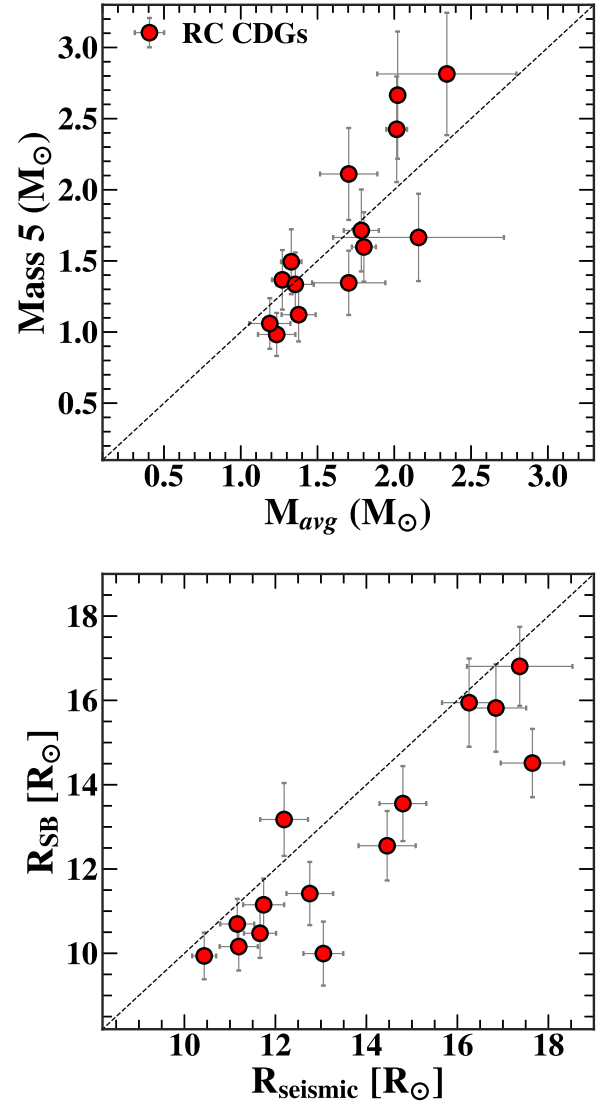


Figure 6. Top panel: comparison of the average seismic masses of the RC CDGs using Equations (1), (3), and (4) (M_{avg} ; see the text for details), vs. the nonseismic masses from Equation (5). The horizontal error bars show the 1σ standard deviation around the average seismic masses for each star. Bottom panel: comparison of the seismic radii and radii calculated from the Stefan–Boltzmann law.

Table 2
Average Uncertainties on the Masses for Each Mass Equations ($\overline{\sigma}$;
Equation (1)–(5))

Mass Equation	$\overline{\sigma} \pm 1\sigma$	$\overline{M} \pm 1\sigma$
1	0.17 ± 0.08	1.77 ± 0.46
2	1.26 ± 0.77	1.39 ± 0.29
3	0.17 ± 0.04	1.50 ± 0.29
4	0.14 ± 0.06	1.68 ± 0.37
5 (nonseismic)	0.27 ± 0.09	1.69 ± 0.55

Note. Also shown are the average of the masses given by each mass equation (\overline{M}). It can be seen that Equation (2) has very large uncertainties. Units are M_{\odot} .

We determine the Li abundances for the 12 stars by matching synthetic spectra with the observed 6707.8 Å line. First, the radial-velocity corrected spectra were continuum-fitted and normalized using the iSpec code (Blanco-Cuaresma et al. 2014;

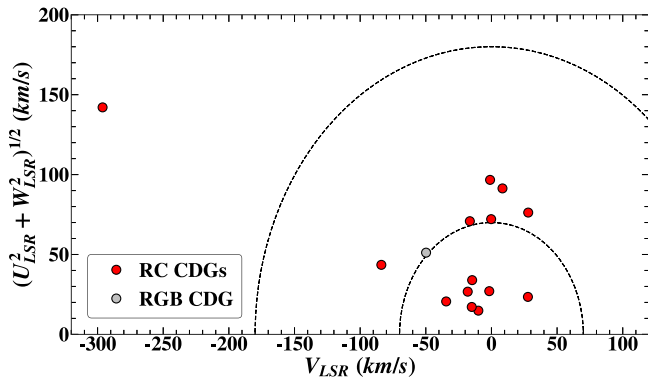


Figure 7. Our CDG sample is shown in the Toomre diagram. Dashed lines show constant values of the total space velocity, $v_{\text{tot}} = (U_{\text{LSR}}^2 + V_{\text{LSR}}^2 + W_{\text{LSR}}^2)^{1/2}$ at 70 and 180 km s^{-1} demarcating thin disk and thick disk components, respectively (Nissen 2004; Venn et al. 2004).

Blanco-Cuaresma 2019). Stellar parameters (T_{eff} , $\log g$, and $[\text{Fe}/\text{H}]$) were taken from the LAMOST catalog for stars with low-resolution spectra and from the APOGEE catalog for the star with the medium-resolution spectrum. The microturbulent velocities (ξ) were derived using an empirical relation for giants from Holtzman et al. (2018). We compiled a line list with associated atomic and molecular data around the Li line using the *linemake* code¹⁰ (Placco et al. 2021).

Local thermodynamic equilibrium (LTE) model atmospheres were generated using the ATLAS9 code (Castelli & Kurucz 2003) for the adopted atmospheric parameters. A series of synthetic spectra were then generated for each star by varying the Li abundance, using the Python wrapper of the 2013 version of LTE radiative transfer code MOOG (Snedden 1973), *pyMOOGi*.¹¹ Finally, the synthetic spectra were matched with the observed spectra. The Li abundance of the best-matched (least χ -square) synthetic spectrum was taken as the LTE abundance for each star. The NLTE Li abundance was then computed following Lind et al. (2009).¹²

We show the derived $A(\text{Li})_{\text{LAMOST}}$ of the CDGs using the LAMOST spectra in Table 3. In the Table, we also present a comparison between $A(\text{Li})_{\text{LAMOST}}$ and $A(\text{Li})_{\text{Literature}}$ of the CDGs. We see good consistency between our measurements and results in the literature.

In total, we found six out of the 12 CDGs with LAMOST spectra to be Li-rich. These stars are also identified as Li-rich in the Yan et al. (2021) study (Table 3). Thus 50% of our sample for which we have spectra is Li-rich. This can be compared to the expected fraction for field stars. First we note that our detection limit, $A(\text{Li}) > 1.8$ dex, is similar to the traditional Li-rich definition, $A(\text{Li}) > 1.5$ dex. Using a GALAH survey sample, Kumar et al. (2020) showed that the fraction of RC stars with $A(\text{Li}) > 1.5$ dex is $\approx 3\%$. Thus, our finding of 50% represents an extremely high fraction—17 times the expected fraction—despite the selection criterion being on carbon, not lithium. Further, for RC stars, it has been shown that stars with $A(\text{Li}) > -0.9$ dex can be considered Li-enhanced, due to Li destruction in the preceding RGB phase (at least for stars in the mass and metallicity range considered in Kumar et al. 2020).

¹⁰ <https://github.com/vmplacco/linemake>

¹¹ <https://github.com/madamow/pymoogi>

¹² Data obtained from the INSPECT database, version 1.0 (<http://www.inspect-stars.com>).

Thus, many more CDGs in our sample may be Li-enhanced if studied with high-resolution spectra—our 50% is a lower limit in this regard. Regardless of the exact proportion, it is clear that Li-richness is highly correlated with C-deficiency. We discuss this further in Section 4.6.

3.6. Bimodality of the RC CDGs

3.6.1. Overluminous and Normal-luminosity Stars

In Section 3.2 we reported a bimodality in the luminosity distribution of our RC CDGs (see Figure 3). The fainter CDGs are in a region bounded by $\log(L/L_{\odot})$ from 1.67 dex to 1.89 dex, which matches well with theoretical predictions of the core He-burning phase for low-mass stars (i.e., $\log(L/L_{\odot}) \approx 1.55\text{--}1.85$ dex; Girardi 2016). This is also clear from Figure 10(a), where we compare our RC CDG sample with a background RC sample—the fainter RC CDGs fall on the normal RC. We will be referring to these stars as “normal-luminosity-RC CDGs.”

The brighter CDGs are more luminous than the typical RC stars: they have $\log(L/L_{\odot})$ between 1.98 dex and 2.17 dex. RC models of masses covering our seismic mass range do not have luminosities this high. Observationally, we see that the bright CDGs are a factor of ≈ 2 brighter than the normal RC for stars of the same mass ($\approx 60 L_{\odot}$ versus $120 L_{\odot}$; Figure 10(a)). We refer to this group as “overluminous-RC CDGs.”

It is possible that the bimodality in the luminosity distribution is an artifact of systematics in our luminosity determination. In Figures 4(c) and 10(d), we show the asteroseismic parameters for our sample. These show correlations with luminosity, with the overluminous stars having low $\Delta\nu$ and ν_{max} . Since luminosity and the seismic parameters are totally independent measurements, this strongly suggests that the bimodality is real. Moreover, in Figure 4(h) we see a very strong correlation with sodium, with the overluminous stars generally having higher Na than the normal-luminosity-RC CDG stars, by an average of +0.25 dex. This further supports that these are two distinct groups of RC stars.

Radius shows an expected correlation with luminosity. On the other hand, mass does not show a significant correlation—both groups roughly cover the same mass range (≈ 1.2 to $2.3 M_{\odot}$), although the normal-luminosity group appears biased to slightly lower masses on average, with $M_{\text{avg}} = 1.5 M_{\odot}$ compared to $1.8 M_{\odot}$ for the overluminous stars.

In the bottom panel of Figure 4 we also show the C, N, and O abundances of our sample versus luminosity. The overluminous stars have slightly lower carbon than the normal-luminosity stars. We find an average carbon abundance of $[\text{C}/\text{Fe}] = -0.7 \pm 0.1$ dex for the former and $[\text{C}/\text{Fe}] = -0.5 \pm 0.1$ dex for the latter. The nitrogen abundances of the overluminous stars are enhanced by an average of +0.1 dex more than the average $[\text{N}/\text{Fe}]$ of the normal-luminosity CDG stars. This is a smaller offset than the average for carbon (-0.2 dex). In contrast, the $[\text{O}/\text{Fe}]$ values of both groups of stars are close to scaled solar, although three overluminous stars appear to be α -enhanced (Section 3.5).

3.6.2. Known CDGs in the Context of Luminosity Bimodality

In the bottom panel of Figure 4 we also show 29 known wG stars from the literature that have carbon abundances from high-resolution optical spectra (Adamczak & Lambert 2013; Palacios et al. 2016). Of these, only six stars have ν_{max} reported in the literature, based on TESS data (Hon et al. 2021). These

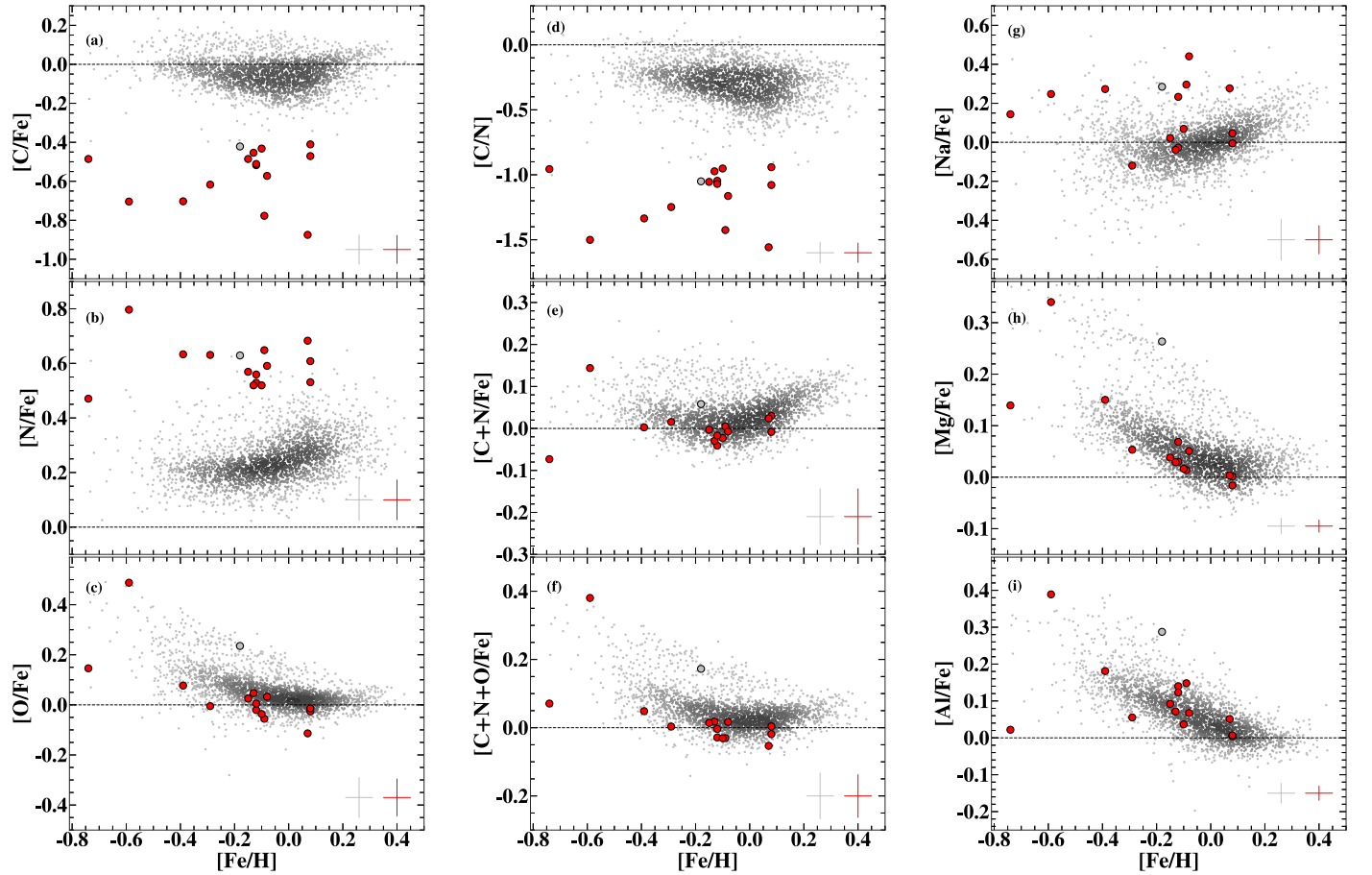


Figure 8. Various CNO abundance ratios and sums along with sodium, magnesium, and aluminium abundances against $[\text{Fe}/\text{H}]$ for our CDGs (large symbols). A large sample of RC stars from Vrard et al. (2016) form the background sample (small circles). All abundances are from APOGEE DR17. Average error bars are shown on the lower right of each subplot. Solar abundances are from Grevesse et al. (2007).

six stars are plotted in the top panel of Figure 4. It can be seen that these known wGb stars have high luminosities and low ν_{max} , similar to our sample of overluminous stars. They also have similar T_{eff} to our luminous sample, and therefore lie in the same region of the HRD in Figure 10(a). This suggests that they are also RC stars, and appear to be the same type of stars as our overluminous-RC CDGs, just with more extreme chemical signatures (Figure 4).

However, despite being overluminous, this literature sample has spectroscopic $\log(g)$ values close to the normal-luminosity stars (average $\log(g) \simeq 2.7 \pm 0.1$ dex; also see Figure 1), and thus appear to be systematically high in $\log(g)$ given their luminosities. We note that the $\log(g)$ values are from the literature, so may have a systematic offset from our sample. No seismic $\log(g)$ is available for this known wGb sample as a cross-check. More data is required to determine the source of this discrepancy. In contrast, the luminosities of these stars are on the same scale as our sample.

Combining ν_{max} with the nonseismic parameters (T_{eff} , L/L_{\odot}), we estimated the seismic masses of these six stars using mass Equation (3). The seismic mass range of these known wGb stars is $1.6 M_{\odot} \leq M \leq 2.9 M_{\odot}$ (with average 1σ uncertainties on the masses of $0.3 M_{\odot}$). With the exception of one star at $\simeq 3 M_{\odot}$, the rest of the sample is consistent with being low-mass ($M \leq 2 M_{\odot}$; Figure 4(b)), similar to our Kepler-APOGEE sample. This is in contrast to previous studies, which have reported that these six known wGb stars

are intermediate-mass stars ranging from $2.9 M_{\odot}$ to $3.3 M_{\odot}$, based on their positions on the HRD (Adamczak & Lambert 2013; Palacios et al. 2016).

As a check, we also calculated the nonseismic masses (mass Equation (5)) for this sample. We found that these masses were substantially higher. In Figure 11 we compare these two mass estimates. We are unsure as to why there are such large differences, but it may be related to the $\log(g)$ -luminosity tension noted above. Further, the uncertainties on the nonseismic masses are generally very large. In fact, four out of the six stars have nonseismic masses within 1.5σ of the seismically determined masses (Figure 11). We note that this discrepancy is not found for our Kepler-APOGEE sample, where the seismic masses are consistent with the nonseismic masses (Figure 6).

In terms of chemical abundances, the six known wGb stars have more extreme chemical patterns than our sample of stars. Their C is more depleted and N more enhanced. Sodium, which is scaled solar in the normal-luminosity group and enhanced by an average of $[\text{Na}/\text{Fe}] = +0.2$ dex in our overluminous group, is further enhanced in the known wGb sample ($[\text{Na}/\text{Fe}] = +0.4$ dex). Oxygen, in contrast with our sample, which is approximately scaled solar, is on average slightly enhanced, with $[\text{O}/\text{Fe}] \sim +0.1$ dex. We are unsure whether this is due to their initial composition being α -enhanced due to their lower average $[\text{Fe}/\text{H}]$, or if it may indicate a further nucleosynthetic product of the pollution episode. This is explored further in Section 4.

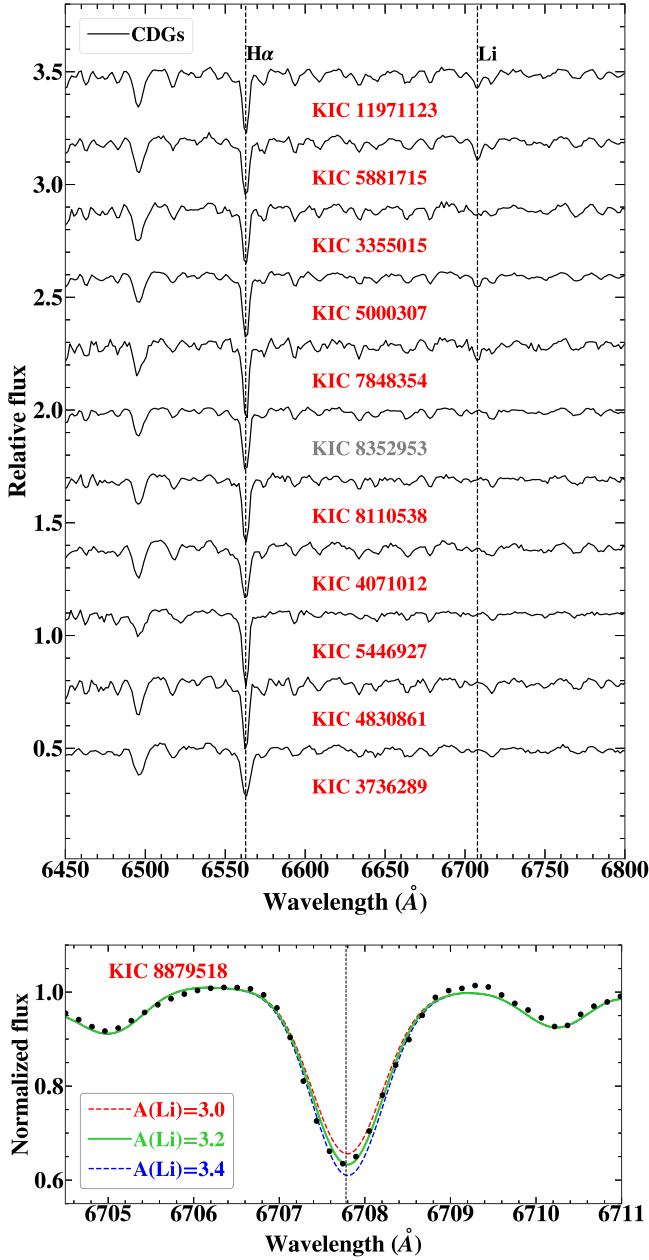


Figure 9. Top panel: LAMOST low-resolution spectra of the CDGs. Note that KIC 8352953 is the only RGB CDG in our sample. Bottom panel: comparison of the observed LAMOST medium-resolution spectra and synthetic spectra of KIC 8879518 for different Li abundances. Synthetic spectra (green solid line) of $A(\text{Li}) = 3.2$ dex best fits the observed spectra. The first five CDGs in the top panel and the CDG in the bottom panel show strong Li absorption lines at 6707.8 Å.

3.6.3. Seismic Data and the Luminosity Bimodality: Masses and Radii

In panels (b) and (c) of Figure 10 we plot seismically derived parameters, following the analysis of Li et al. (2022) into underluminous and stripped stars. We note that in all panels of Figure 10, our overluminous-RC CDGs are concentrated in regions far from the normal (background) RC stars. This is true for panel (a), which is based on photometric data, and also panel (c), which is entirely based on seismic data. As mentioned above, the fact that the overluminous-RC CDGs stand out in diagrams with totally independent data (and in chemistry; see Figure 4) is a very strong indication that the bimodality is real.

Table 3

Derived NLTE Lithium Abundances for Our CDGs from LAMOST Spectra

KIC	$A(\text{Li})_{\text{Literature}}$ (dex)	$A(\text{Li})_{\text{LAMOST}}^{\text{a}}$ (dex)
5000307	2.7 ^c	2.6
5881715	$3.4 \pm 0.1^{\text{d}}$	3.4
7848354	3.7 ^d	3.3
11971123	2.9 ^d	2.9
3355015	1.9 ^d	2.1
5446927	...	<1.8
4071012	...	<1.8
3736289	...	<1.8
8110538	...	<1.8
8352953	...	<1.8
4830861	...	<1.8
8879518 ^b	$3.5 \pm 0.1^{\text{e}}$	3.2

Notes. Typical uncertainties are ± 0.2 dex.

^a This work.

^b Only has LAMOST medium-resolution spectrum.

^c Silva Aguirre et al. (2014).

^d Yan et al. (2021).

^e Singh et al. (2021).

The reason the overluminous-RC CDGs stand out in panel (c) is because they have low ν_{max} and low $\Delta\nu$ for their masses, given their phase of evolution. This suggests that they have different structures compared to normal RC stars in the same mass range. The middle panel of Figure 10 shows that the majority of these stars also have abnormally large radii, with the four largest stars (out of six) having an average radius of $R_{\text{avg}} = 17.0 \pm 0.8 R_{\odot}$ compared to the background sample with $R_{\text{avg}} = 11.5 R_{\odot}$ in the mass range of interest. Thus, there is a radius difference of $\simeq 5.5 R_{\odot}$. Of the other two stars, one has a high radius for its mass (although not as big a difference as the others), and the other has a radius consistent with normal RC stars.

The normal-luminosity-RC CDGs (eight stars) mostly have normal RC radii ($R_{\text{avg}} = 11.7 \pm 0.4 R_{\odot}$)¹³, although there is one outlier that has a large radius. Also, one star has a slightly lower radius than expected for the RC. This star (KIC 5000307) is classified as an underluminous star (partially stripped) by Li et al. (2022). Although it does stand out in the seismic diagram, we find its luminosity to match that of normal RC stars (Figure 10(a)).

We note that the overluminous-RC CDGs in all panels of Figure 10 coincide with the position of stars in the helium subflashing phase as defined by Mosser et al. (2014). We discuss this in Section 4.4.1.

Finally, as mentioned above, the normal- and overluminous groups cover roughly the same mass range. However, we see in Figure 10(b) that both groups have higher average masses than the background RC sample. In particular, there are no RC CDGs below about $1.2 M_{\odot}$. Further, the overluminous stars appear biased to slightly higher masses ($M_{\text{avg}} = 1.8 M_{\odot}$), while the normal-luminosity stars have an average mass of $1.5 M_{\odot}$. Being relatively massive is suggestive of a merger-product population, which we discuss in detail in Sections 4.4.2 and 4.5.2.

¹³ This average ignores the outlier.

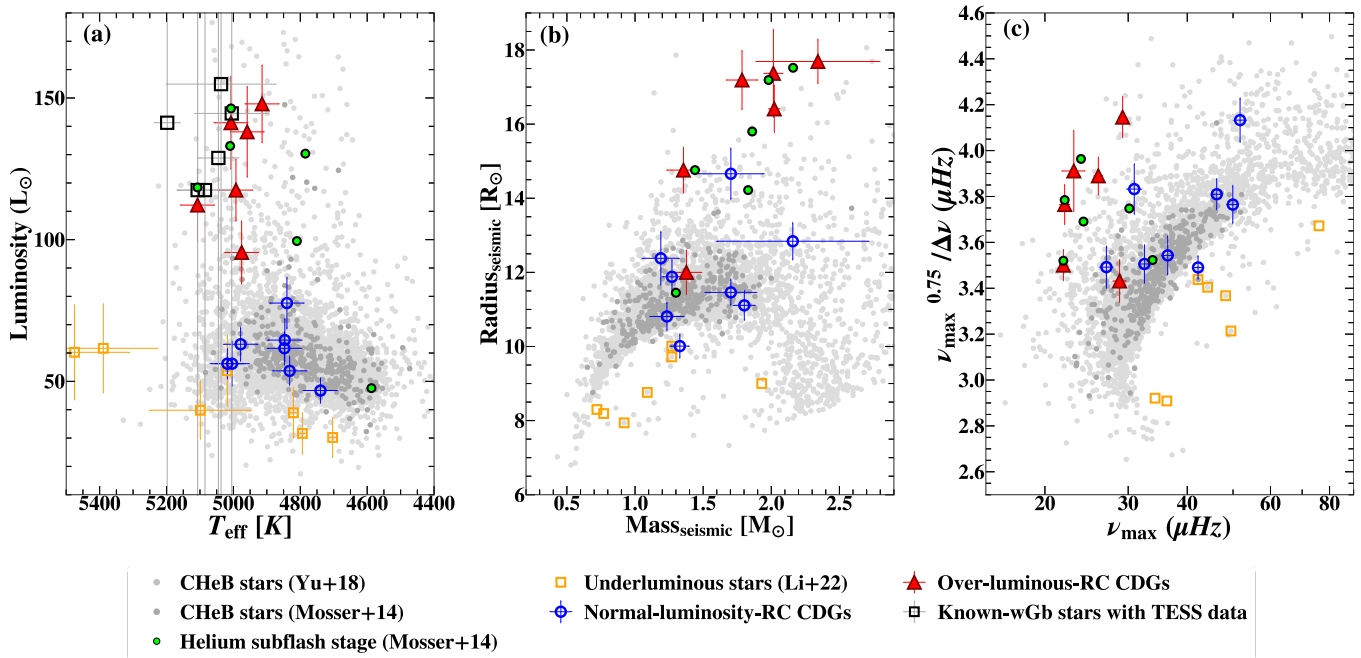


Figure 10. (a) The Hertzsprung–Russell diagram. (b) The mass–radius diagram. (c) The seismic quantity $\nu_{\max}^{0.75} / \Delta\nu$ vs. ν_{\max} . The RC stars classified based on asteroseismic analysis form the background from Mosser et al. (2014) and Yu et al. (2018; small filled gray and silver circles, respectively). The helium subflash stars from Mosser et al. (2014) are represented by small filled green circles. The underluminous stars from Li et al. (2022) are shown by orange squares, the known wGb stars are shown by black squares, and the normal-luminosity-RC CDGs and the overluminous-RC CDGs from our study are shown by blue circles and red triangles, respectively.

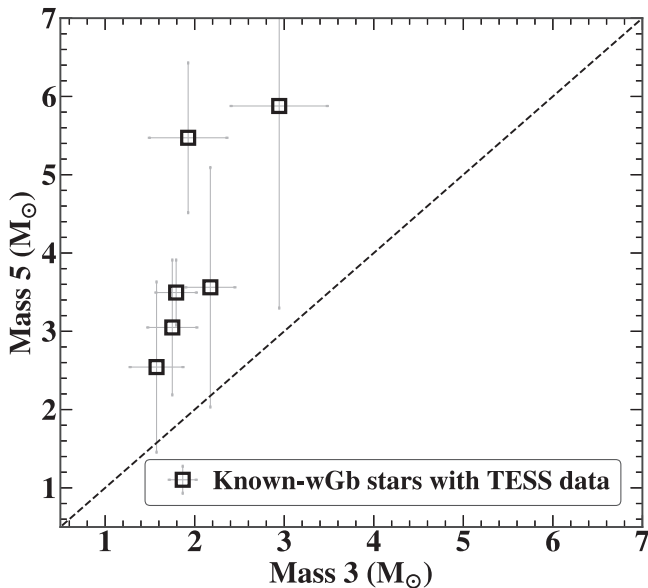


Figure 11. Comparison of the seismic masses of the previously known wGb stars with TESS data determined using Equation (3), vs. their masses determined using the nonseismic mass Equation (5).

4. Discussion

The first dedicated spectroscopic survey for C-deficient stars was undertaken 50 yr ago by Bidelman & MacConnell (1973), who found 34 wGb/CDG stars. This sample has comprised 77% of the wGb stars studied through the decades (e.g., Cottrell & Norris 1978; Sneden et al. 1978; Parthasarathy & Rao 1980; Palacios et al. 2012; Adamczak & Lambert 2013). Bond (2019) added five more wGb stars identified via spectroscopy. The primary aim of the current study was to better characterize the CDGs since they are still poorly understood.

4.1. Overview of Our Results

To better characterize the CDGs, we took advantage of the high-quality asteroseismic data of the Kepler field, which allows for mass and evolutionary-phase determinations, combined with data from large spectroscopic surveys that overlap with the Kepler field (APOGEE and LAMOST), which provide abundances and stellar parameters. Here we enumerate our key results, and we discuss the implications of these findings further below.

1. To date, there has been no strict definition for CDGs in the literature. We developed a definition for CDGs based on stellar model predictions and a large spectroscopic sample. Standard stellar models do not deplete carbon below ≈ -0.3 dex (taking into account lower-than-average initial abundances), and we consider stars with $[C/Fe] < -0.4$ dex as carbon deficient.
2. Our sample adds 15 new CDGs to the literature. All of our CDGs are in the Kepler field. They have quality abundances, asteroseismic masses, and evolutionary phases.
3. Considering our new seismic masses, most of our CDGs are low-mass stars, that is, stars that are expected to have gone through the core helium flash ($M \lesssim 2 M_{\odot}$). Taking into account mass uncertainties of the two most-massive stars in the sample, 100% of the sample is consistent with being low mass ($1 M_{\odot} - 2 M_{\odot}$). This is at odds with the previous understanding in the literature, where wGb stars were considered to be of intermediate mass ($M = 2.5 M_{\odot} - 5.0 M_{\odot}$), which do not experience the core helium flash.
4. Remarkably, we conclude that 93% of our CDGs are in the RC phase—14 out of 15 stars—with only one being an RGB star. This is strongly supported by our subsample

of 11 stars for which we have asymptotic g-mode values $\Delta\Pi_1$, 100% of which were found to be RC stars (Figure 2).

5. Two out of the 11 stars (18%) for which we have $\Delta\Pi_1$ measurements are in the helium subflashing phase according to Mosser et al. (2014). This is 4.5 times the expected percentage (3.8%) found in our background sample of RC stars. Both stars are overluminous-RC CDGs. Moreover, in the seismic diagram of Figure 10, almost all of the overluminous-RC CDGs are found in the same region as the subflashing stars.
6. We found that the CDGs are universally N-enhanced. Analysis of CNO sums showed that the material in the envelopes of our CDG stars has been processed through the CN cycle, and likely not the ON cycle. The fact that $[C+N+O/Fe]$ is scaled-solar indicates that no He-burning products have been involved in the pollution event(s) (although this is not true for the literature sample in Section 4.2.2).
7. We find a strong correlation between stars being C-deficient and Li-rich, with six out of 12 CDGs (50%) for which we have low-resolution spectra being Li-rich. This is 17 times higher than the expected fraction of 3%.
8. We find a bimodality (roughly 60:40) in luminosity within our sample, with the normal-luminosity-RC CDGs (60% of the sample) having an average luminosity of $\log(L/L_\odot) \simeq 1.8$ dex ($60 L_\odot$), and the overluminous-RC-CDGs having an average luminosity of $\log(L/L_\odot) \simeq 2.1$ dex ($120 L_\odot$). Given their low masses, the overluminous-RC-CDGs are significantly more luminous than expected, by a factor of about 2.
9. On further investigation, we found the luminosity groups to also be distinct in Na abundance, with the normal-luminosity-RC CDGs having scaled solar Na but the overluminous-RC CDGs having on average $[Na/Fe] \sim 0.3$ dex. This is a factor of about 1.5 greater than expected from FDU. The luminosity groups also strongly correlate with radius and the asteroseismic parameters, with the more luminous stars having lower $\Delta\nu$ and lower ν_{\max} . In addition, the overluminous-RC-CDGs have lower carbon and higher N than the normal-luminosity-RC CDGs, indicating more extreme pollution.
10. Comparing our sample with the previously known wGb stars for which we have some seismic data (TESS), we found that the latter are also primarily low-mass stars and are overluminous for their masses. Thus, they appear to be members of our overluminous-RC group. They however show signs of having undergone even more extreme pollution.

4.2. Characterization of Carbon-deficient Stars

4.2.1. Three Groups of CDGs

As reported in Section 3.6 (also see points 9 and 10 above), our CDGs appear to fall into two distinct groups: normal-luminosity-RC and overluminous-RC stars. Before we discuss the possible formation theories for CDGs, here we explore the differences between these groups further and compare to other, previously known CDGs in the literature.

In Figure 12 we show $[Na/Fe]$ versus the sum $[C+N+O/Fe]$ for various stellar samples. We see here that our two luminosity groups are clearly separated in Na. However, they are not

separated in $[C+N+O/Fe]$, with both showing scaled-solar composition. By contrast, the known wGb stars for which we have seismic data (open squares, six stars) are enhanced in Na but also in $[C+N+O/Fe]$ (by an average of +0.2 dex). A larger literature sample, which has no seismic data (filled circles, 23 stars), is also shown in Figure 12. These stars overlap with our sample—they are also simultaneously Na-rich and CNO-rich. Thus, it appears that the CDGs fall into three groups.

To further investigate these possible groupings, we collate all key information we have from the current study: abundances, masses, and luminosities. The groupings do appear to be distinct—we display the characteristics for each in Table 4, and include the nonseismic literature sample as Group 3b. In this table, we see a clear progression from lower luminosities to higher luminosities, along with lower masses to higher masses, although there is a significant overlap between the groups. There is also a progression of C-depletion (N-enhancement) through the groups. Oxygen is only enhanced in Group 3. Lithium is anticorrelated with Na in the first two groups, with the normal-luminosity-RC CDGs being Li-rich but the overluminous-RC CDGs not. At the more-massive/luminous end (Group 3), Li-rich stars appear again.

4.2.2. Chemical Signatures in the Groups

Having $[C+N+O/Fe] > 0.0$ is a signature of He-burning products being mixed up to the envelope, while $[C+N+O/Fe] = 0.0$ is a signature of CN(O) cycling only, since in this case the CNO elements are just transmuted within the cycle (primarily to N). Given a scaled-solar starting composition during a CNO burn, there is a limit to which N can be enhanced via the CN cycle. As an estimate, taking the extreme limit where all C is burned to N, we would expect $[N/Fe]$ to reach its upper limit at $\simeq +0.6$ dex. If the ON cycle were activated, higher N abundances would be possible. Given that our sample of CDGs (Groups 1 and 2) generally has scaled-solar oxygen (Figure 8; Table 4) and $[C+N+O/Fe] = 0.0$, it appears the ON cycle was not activated in these stars. However, due to the very high initial abundance of O, it would take very little ON burning to increase the N. Taking a typical uncertainty on the O abundances as $\simeq 0.1$ dex, a rough calculation shows that a hidden (within uncertainties) 0.1 dex depletion in O would increase $[N/Fe]$ by another 0.2 dex, to $[N/Fe] = 0.8$ dex. We indicate this limit in Figure 13 (vertical shaded band, since it is approximate), which shows the C and N distributions of all of the CDG groups. The limit matches well with the observed upper $[N/Fe]$ limit of our CDGs. Any stars with $[N/Fe]$ above this limit must have been enhanced in CNO elements at some stage.

The previously known CDGs with TESS seismic data (open squares in Figures 12 and 13; Group 3a in Table 4) have much higher N abundances than our Group 1 and 2 stars, starting at $[N/Fe] \simeq +1.0$ dex and increasing to $\simeq 1.3$ dex. Thus, there appears to be a nitrogen gap between Groups 1+2 and Group 3. Given Group 3 is above the $[N/Fe]$ limit of +0.8 dex for complete burning of C to N, these stars must have had CNO elements added to their envelopes, likely through dredge-up of He-burning products. This aligns with their overabundances of $[C+N+O/Fe]$ (Figure 12 and Table 4). However, the fact that the N is so high (and C so low) in the CNO-enhanced group indicates that there has been very strong hydrogen burning on top of this. This is supported by the low $^{12}C/^{13}C$ and very low $[C/N]$ (see Table 4), both indicating equilibrium CN(O) cycling. To reach CNO equilibrium typically takes about 10^4 yr

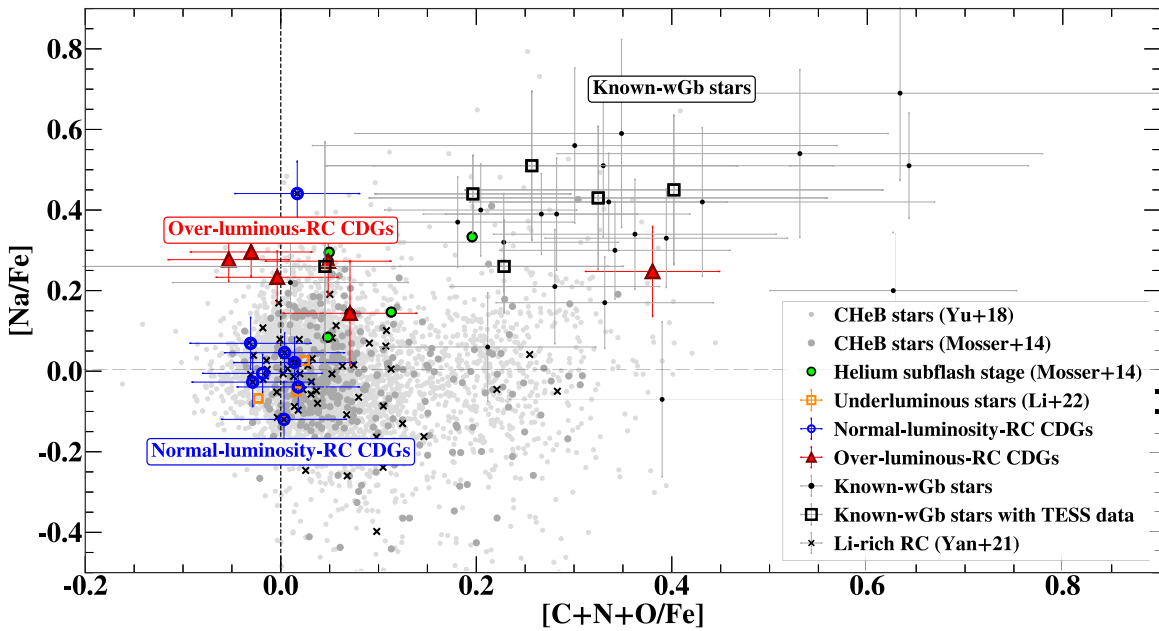


Figure 12. Trends of sodium abundance vs. the $[C+N+O/Fe]$ abundance ratio. Giants classified based on asteroseismic analysis form the background from Mosser et al. (2014) and Yu et al. (2018; small filled circles; see key). The underluminous stars from Li et al. (2022) are shown by orange squares. The abundance ratios of the normal giants and the underluminous stars are from APOGEE DR17. The normal-luminosity-RC CDGs, and the overluminous-RC CDGs from our study are represented by blue circles and red triangles, respectively. Large black squares are the previously known wGb stars that have asteroseismic data from Hon et al. (2021), and the small black circles are the rest of the known wGb stars from literature with carbon abundances from high-resolution spectra. The Li-rich giants (black crosses) are from the Yan et al. (2021) study. These Li-rich giants are the low-spectral-resolution RC sample that have good-quality APOGEE DR17 data. In total, we have a sample of 59 Li-rich RC stars for comparison with the CDGs. Six of our normal-luminosity-RC CDGs are included in the Li-rich study of Yan et al. (2021). We use the solar abundance of C, N, O, and Na as derived by Grevesse et al. (2007).

Table 4
Comparison of Our Classifications of the CDGs

	Group 1 (Normal-luminosity RC)	Group 2 (Over-luminous RC)	Group 3a (TESS)	Group 3b (Lit.)
Lum. (L_{\odot})	50–80	95–150	120–155	110–760
Mass (M_{\odot})	1.2–2.2	1.4–2.4	1.6–3.0	...
$[Na/Fe]$	0.0	+0.3	+0.4	+0.4
$[CNO/Fe]$	0.0	+0.1	+0.2	+0.4
Li-rich frac.	90%	0%	85%	40%
$[C/Fe]$	−0.5	−0.7	−1.3	−1.1
$[N/Fe]$	+0.5	+0.6	+1.1	+1.3
$[O/Fe]$	0.0	+0.1	+0.1	+0.2
$[C/N]$	−1.1	−1.3	−2.4	−2.4
$^{12}C/^{13}C$	6	5
$[Fe/H]$	−0.1	−0.3	−0.2	−0.2

Note. Approximate averages and ranges are given. See the text for the definition of each sample/group. The ellipses indicate that data is not available.

(Caughlan 1965). This puts a time constraint on the minimum burn time for the event that gave rise to the chemical pattern in Group 3. Sodium is also enhanced, which is also expected for hot hydrogen burning. This suggests the burn temperature was high enough to activate the NeNa chain at around 50–60 MK (Arnould et al. 1999). We note that this chemical pattern is very similar to that of hot bottom burning (HBB) on top of third dredge-up (TDU) in AGB stars (e.g., Karakas & Lattanzio 2014; see discussion in Section 4.4.3). Any pollution scenario would need to reproduce HBB conditions, at least for Group 3 stars. This may be achieved, for example, by stellar mergers, as discussed below (Section 4.4.2).

Turning to the Group 1 and 2 stars, they are distinguished by having $[C+N+O/Fe]$ approximately unchanged from their initial scaled-solar values. This indicates that, unlike Group 3, the polluting material was not enriched in He-burning products through core dredge-up. The degree of N-enhancement/C-deficiency depends on the amount of burning that the material underwent (along with any dilution that may have occurred if the pollution was from an external source). Given their high $[N/Fe]$ and low $[C/Fe]$, these stars show signs of substantially progressed CN(O) burning. We do not have $^{12}C/^{13}C$ for them, but the $[C/N]$ is low (Table 4). However, as shown by Clayton (1983), we expect $[C/N] \approx -2.5$ dex in equilibrium CN(O) burning at around 30–50 MK, which is much lower than the observed -1.1 to -1.3 dex in these stars. Thus, it appears that equilibrium was not quite reached during the burning that gave rise to the patterns in these stars. Since it takes about 10^4 yr to reach equilibrium (Caughlan 1965), this puts a time constraint on the maximum burn time for the Group 1+2 chemical patterns. The $[C/N]$ ratio is higher in Group 1, which could be due to a lower-temperature burn. Further, Na is not enhanced in Group 1 while it is in Group 2. This suggests that the burn temperatures were around 20–40 MK (Adamczak & Lambert 2013) in Group 1 but around 50–60 MK in Group 2. This may have allowed Li to survive in the Group 1 stars, as opposed to Group 2 (Table 4; also see Li discussion in Section 4.6).

4.3. Revisiting Previous Theories on the Origin of C-deficient Stars

Before the current study, the general picture of the nature of wGb/CDGs was that:

1. Most have uncertain evolutionary status (SGB, RGB, RC, and EAGB).

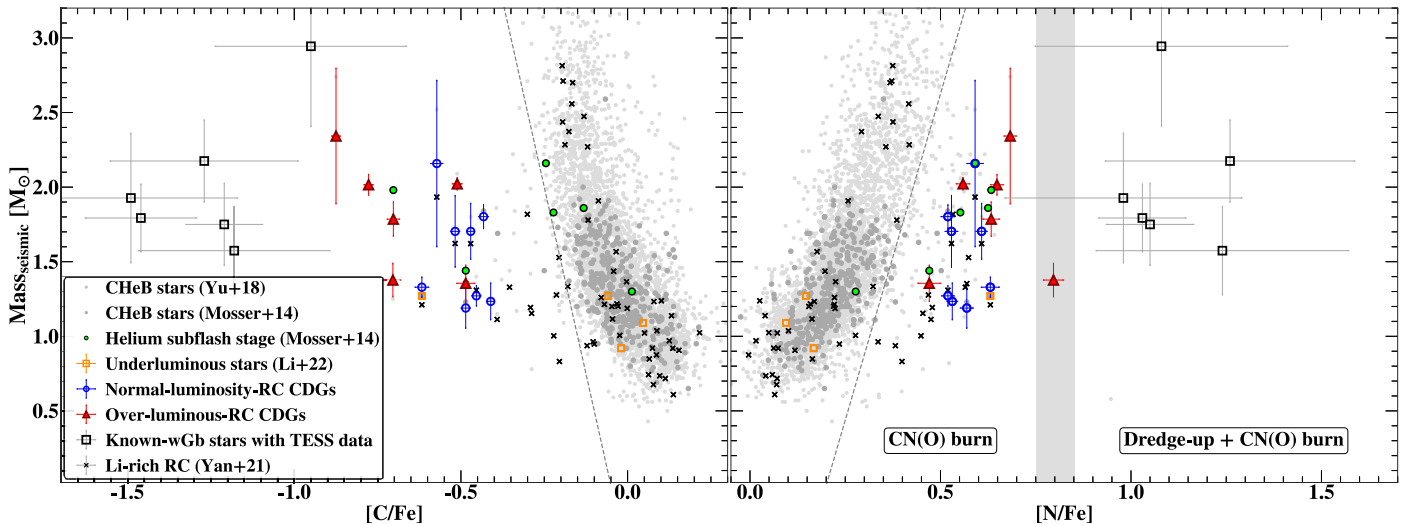


Figure 13. Seismic mass vs. $[C/Fe]$ (left panel); seismic mass vs. $[N/Fe]$ (right panel) for our CDGs, the previously known wGb stars, underluminous stars from Li et al. (2022), Li-rich giants from Yan et al. (2021), and a large sample of RC stars from Mosser et al. (2014) and Yu et al. (2018) with symbols having the same meaning as in Figure 12. We determine luminosities for the Li-rich giants in the same manner as our CDGs, detailed in Section 3.2. Using this, we estimated the seismic masses of these stars using mass Equation (3). Six of our normal-luminosity-RC CDGs are included in the Li-rich study of Yan et al. (2021). They overlap with the Li-rich giants with a slight offset in seismic mass. The “normal” RC stars show a correlation between mass and nitrogen (and carbon) abundance. This reflects FDU surface pollution from early on in the RGB (e.g., Iben & Renzini 1984). The trend shows fairly sharp edges, allowing us to make a cut in N (or C) that varies with mass (dashed lines). This helps in distinguishing the chemically peculiar stars. To the right of the N line, the stars can be considered N-rich, for their mass. The vertical shaded region at $[N/Fe] = +0.8 \pm 0.05$ dex, denotes the upper limit of our CDG sample’s N-enhancement as well as the highest N abundance possible if the ON cycle was activated after all C is burned to N (see the text for details). Solar abundances are from Grevesse et al. (2007).

2. They are intermediate-mass stars ($M \approx 2.5 M_{\odot} - 5.0 M_{\odot}$).
3. They may mainly be thick-disk objects given their large distances from the Galactic plane.
4. All have N overabundances.
5. Some are enhanced in Li.
6. Most are enhanced in Na.
7. All of those measured have low $^{12}\text{C}/^{13}\text{C}$ ratios.

For seven decades, the precise evolutionary state of the CDGs/wGb stars has been uncertain. This is due to the fact that they are found in a very crowded area of the HRD where it is difficult to distinguish between various evolutionary phases (SGB, RGB, RC, and EAGB).

By taking advantage of the Kepler asteroseismic data, our study shows conclusively that almost all (14/15) of our sample of stars are in the RC (core He-burning) phase. For our previously known CDG sample with data, for which we have only ν_{\max} , we find they are also consistent with being RC stars (Figure 4). Considering the wider literature sample of CDGs, we find that many of them are consistent with RC luminosities but there is also a subset that has much higher luminosities (black dots in Figure 4).

The fact that there are very few stars below the RC luminosity—we have one single example out of 44 stars (15 Kepler CDGs + 29 known CDGs; Figures 1 and 4)—means that the CDG chemical signature could not have arisen before the RGB bump (since the bump has roughly the same luminosity at the RC). Further, if almost all CDGs are RC stars (we require more seismic data to determine this), the pollution event could not have occurred before the RGB tip (except in a merger scenario; see Section 4.4.2). This important new finding helps constrain theories of the origin of the CDGs. Theories that suggest that the chemical pattern was imprinted during the PMS or MS are not supported by this new evidence. This applies to self-enrichment theories (e.g., self-enrichment through rapid rotation; Adamczak & Lambert 2013) and also external pollution theories, for example,

where the chemical pattern is thought to reflect the birth composition of the stars, whereby they could have been born polluted or have been polluted in their infancy by more-massive stars that would have ejected CNO cycle processed material (Palacios et al. 2016). Previous studies did note that these theories have their weaknesses; for example, there were no known MS stars with the same chemical pattern as the CDGs that could have been progenitors. We note that we also did not find any MS or SGB C-deficient stars (Figure 1), further suggesting that the pollution event does not happen early in the evolution.

Another possible theory in the literature is that CDGs are products of mass transfer or merger events (Bond 2019). This is based on three pieces of evidence: (i) the systematically high distances from the Galactic plane as compared to normal red giants lying in the same location in the CMD, (ii) their apparent higher masses ($2.0 - 4.5 M_{\odot}$), which might imply they are binaries or binary products, and (iii) a subset having high rotation rates. In contrast, for our sample (for which we have high-quality seismology) we find that: (i) there is no preference for the Galactic location of these CDGs (Figure 7; Table 1), and (ii) our CDGs are predominantly low-mass stars ($1.2 - 2.3 M_{\odot}$; Figure 6). Due to these findings, it can be seen that the Bond (2019) theory of CDGs belonging to a special stellar population may not apply to our sample. Although the masses of our sample are relatively low, we note that they still appear biased toward higher masses, just not as strongly. We consider the merger scenario for our sample in light of our new constraints in Sections 4.4.2 and 4.5.2.

As a caveat, we note that in Section 3.6.1 we reported seismic masses for six stars from the literature. Five out of six of these stars were in the Bond (2019) study. As mentioned in Section 3.6.1, there is a tension between our seismic masses, which are generally low, and our nonseismic masses, which are generally higher (Figure 11). This adds some uncertainty around the formation scenario(s), for this subset of stars.

4.4. Possible Explanations for the Origin of Group 2 and Group 3 CDG Stars Based on Our New Findings

4.4.1. Overluminous-RC CDGs (Group 2): Helium Subflashing Stars?

At the tip of the RGB, low-mass stars go through the core helium flash. After this, they undergo a series of weaker He-flashes as they descend down to the RC luminosity (Bildsten et al. 2012; Singh et al. 2021), where they then spend $\approx 80\text{--}100$ Myr. As mentioned above, two out of the 11 stars (18%) for which we have $\Delta\Pi_1$ measurements are in the helium subflashing phase according to Mosser et al. (2014). This is 4.5 times the expected percentage (3.8%) found in our background sample of RC stars. Also, both stars are overluminous-RC CDGs (Table 4 and Figure 4), and in the seismic diagram of Figure 10 almost all of the overluminous-RC CDGs are found in the same region as the subflashing stars. Thus, it is tempting to associate our overluminous-RC CDGs with stars currently undergoing helium-burning subflashes.

The time spent in subflashes (with convective He-burning shells) is very short ($\approx 10^4$ yr; Bildsten et al. 2012; Singh et al. 2021), so it is very unlikely to find stars in this phase. If these stars are in the subflashing phase then they will soon evolve to the RC. Since our overluminous-RC CDG stars are C-deficient, this would mean that we would expect to see large numbers of C-deficient RC stars, which we do not. Given this, it appears that our overluminous CDGs cannot be subflashing stars. Their location in the seismic diagram (Figure 2) is likely degenerate with other phases of evolution—or different stellar structures, as discussed in Section 4.4.2.

Another argument against these stars being subflashing stars is that, theoretically, it is expected that any mixing at the core helium flash would result in an *increase* in carbon at the surface (e.g., Deupree & Wallace 1987; Izzard et al. 2007; Mocák et al. 2009). However it has been suggested that Li-rich stars may provide evidence for flash-induced mixing without CNO enrichment (Section 4.6).

4.4.2. Overluminous-RC CDGs (Group 2): Merger Products?

Our results show that our overluminous-RC CDGs (Group 2 in Table 4) stand out in a number of ways:

1. Critically, they are more luminous than expected for low-mass RC stars, by a factor of about 2 ($\approx 60 L_\odot$ versus $120 L_\odot$; Figure 10).
2. They have higher average masses than our background RC sample. In particular, there are no stars below $1.35 M_\odot$ (Figure 10).
3. The majority of these stars also have abnormally large seismically measured radii (middle panel of Figure 10) with the four largest stars (out of six) having an average radius of $17.0 \pm 0.8 R_\odot$, which is $\approx 5.5 R_\odot$ larger than the background sample of RC stars ($R_{\text{avg}} = 11.5 R_\odot$ in the mass range of interest).
4. These stars have more extreme chemical patterns than the normal-luminosity-RC CDGs (Group 1 in Table 4). In particular, they show Na enrichment ($[\text{Na}/\text{Fe}]_{\text{avg}} = +0.3$ dex) whereas the normal CDGs have scaled-solar Na. For C and N, our overluminous-RC-CDGs are 0.2 dex more C-deficient and 0.1 dex more N-rich (Table 4 and Figure 4).
5. They also stand out in the seismic diagram of Figure 10, well away from the normal RC distribution.

The combination of their relatively high masses (compared to normal RC stars), higher luminosities, and radii (for their masses) suggests that these stars may be merger products. This was proposed by Bond (2019) for their sample of CDGs. Our seismic information strengthens the fact that these stars are quite different to normal RC stars. In Figure 10 we depict five of the Bond (2019) stars (with seismic parameters). They appear to be equivalent to our overluminous-RC CDGs, although their C depletion is even stronger (and N, Na more enhanced). The Bond (2019) sample being more chemically extreme may be due to selection bias through how they were discovered. They were classified based on the weak CH-band in the spectra recorded in objective prism plates (Bidelman 1951; Bidelman & MacConnell 1973).

As discussed in Section 4.2.2, the chemical pattern seen in these stars reflects previous hydrogen burning through the CN (or CNO) cycle, and the presence of Na indicates that the NeNa chain was also running. This suggests the burn temperature was around 50–60 MK (Arnould et al. 1999). Adamczak & Lambert (2013) also noted that some CDGs have unusually high Li abundances, indicating Li production presumably through the Cameron–Fowler mechanism. On the other hand, our sample of overluminous-RC CDGs (Group 2 in Table 4) does not contain any very Li-rich stars (all stars for which we have spectra have $A(\text{Li}) < 1.8$ dex; Table 3). This is in stark contrast to our normal-luminosity-RC CDG sample (Group 1) of which $\approx 86\%$ are very Li-rich (six out of seven stars; we have spectra for seven out of eight stars of this sample; Table 3).

If we accept the merger scenario for these overluminous-RC CDGs and combine it with our result that virtually all of the CDGs are at the RC luminosity or brighter, the burning must have happened during or after the merger event. That is, since the chemical pattern is not seen in earlier phases of evolution, the simplest explanation is that it arises as a result of the merger event.

Interestingly, in the low-mass merger models of Zhang & Jeffery (2013), there is a case in which CN(O) and NeNa nucleosynthesis does indeed occur (their model B2). Although this model did not match the chemical patterns of the stars they were studying (early-type R and J stars; carbon-rich), they suggested that this type of merger could help explain the globular cluster abundance anomalies, which show a similar chemical pattern to the CDGs. Their model produces stars with surface abundances $[\text{C}/\text{Fe}] = -1.15$ dex, $[\text{N}/\text{Fe}] = 0.88$ dex, $[\text{O}/\text{Fe}] = -0.10$ dex, and $[\text{Na}/\text{Fe}] = 1.42$ dex. Qualitatively, this appears to match the abundances of the overluminous CDGs. They mentioned that Li is at first produced, but quickly destroyed. Their model B2 is a merger between a helium white dwarf ($0.2 M_\odot$) and an RGB star with a He core mass of $0.3 M_\odot$. This is a common formation channel as shown by binary population synthesis (e.g., Izzard et al. 2007). In the B2 model case of Zhang & Jeffery (2013), accretion is from the HeWD onto the RGB helium core.

The full evolutionary picture is shown in Figure 14. Once a HeWD + RGB binary has formed, the RGB star eventually expands and overflows its Roche lobe, leading to a common envelope event. It is assumed that the HeWD merges with the RG core, which means that spiral-in must occur faster than envelope ejection. The resulting merged star has a He-rich core of $0.5 M_\odot$ with a H-rich envelope. The Zhang & Jeffery (2013) B2 model accretes enough envelope mass to make a total merged-star mass of $2 M_\odot$. Evolving the model forward, it

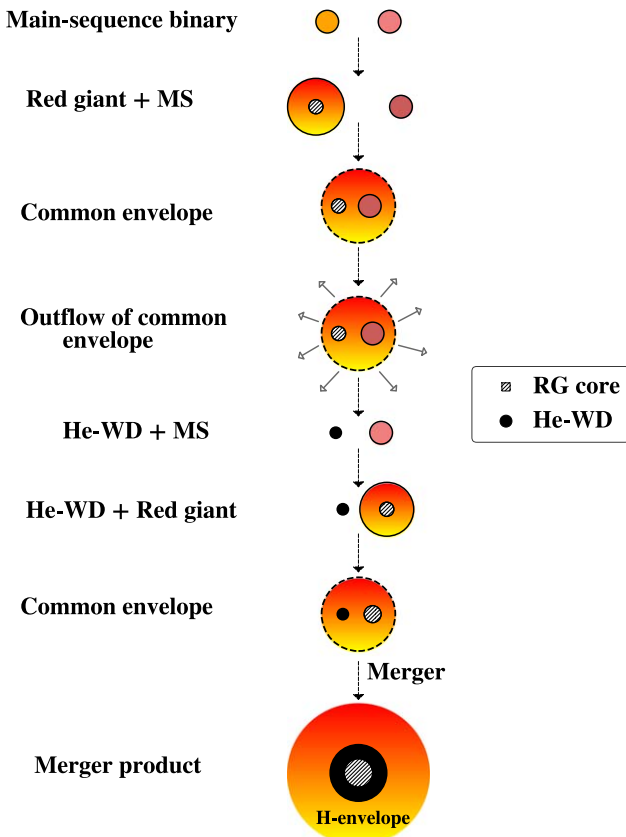


Figure 14. Schematic representation of the possible steps in a HeWD plus RGB star merger leading to the formation of a red clump star with a carbon-poor and nitrogen-rich surface. This illustration is based on Figure 5 in Postnov & Yungelson (2014) and Figure 2 in Zhang & Jeffery (2013).

underwent some strong burning at the base of the convective envelope, which reaches right down to the H-burning shell (their Figure 8). The study did not report the temperature of the envelope burning; however, it can be expected to be in the range 50–70 MK judging from the nucleosynthesis that occurs. The burning lasts about 3 Myr, at which point it undergoes a series of He-shell flashes before settling into convective-core helium burning (RC), where it remains for ≈ 50 Myr. It is this RC phase that we associate with our observed sample of overluminous-RC CDG stars—they have higher-than-normal luminosities, a similar chemical pattern, and are core-helium burners (RC, as identified through Kepler asteroseismology; see Section 3.1). Although there is not an exact quantitative match between our abundances and this particular merger model, it can be expected that a change in model parameters (e.g., HeWD mass, RG core mass), will lead to a variation in burning products due to different thermal structures.

As for the previously known wGb stars for which we have some seismology (Group 3a in Table 4; open squares in Figures 4 and 10), they appear to be members of our overluminous-RC group, with slightly more extreme chemical patterns (Section 3.6.1), so they also fit this merger scenario.

In Figure 4 we also show an extended literature sample of CDGs (Group 3b in Table 4), for which we do not have asteroseismic data. These stars show similar extreme abundance patterns as the known sample for which we have data. However, they show a wide distribution in luminosity, reaching far above the RC luminosity (and above the overluminous-RC). One interpretation of these much brighter stars is that they are

evolved versions of the RC stars (early-AGB). However, if this were the case, then we would expect to see bright CDGs with C-depletion similar to the normal-luminosity and overluminous-RC CDGs (i.e., lying directly above these stars in the leftmost plot of the lower panel of Figure 4), but we do not observe this. Lacking data to confidently assign evolutionary status, we speculate that the bright extension of CDGs are also merger-product RC stars, and the increase in luminosity is due to increasing mass. More data is required to test this hypothesis. We note that these stars may be overrepresented in the literature sample due to their brightness.

We conclude that a merger between a helium white dwarf and a red giant can explain the overluminous-RC CDGs (Group 2), and possibly the bright extension seen in the literature sample of wGb stars (Group 3).

4.4.3. Previously Known wGb Stars (Group 3): AGB Mass Transfer Pollution?

As mentioned in Section 4.2, AGB stars that are undergoing HBB on top of TDU can qualitatively reproduce the chemical pattern in the Group 3 stars. In particular, stars of $\approx 6 M_{\odot}$ produce Na and Li (the Li-rich phase is transient; Karakas & Lattanzio 2014), as well as increasing [C+N+O/Fe], as observed in these CDG stars (Table 4). However, the luminosity range of our sample ($\sim 10^2$ – $10^3 L_{\odot}$) is not compatible with HBB AGB stars ($\sim 10^4 L_{\odot}$). Also, the CDG masses are not as high as $6 M_{\odot}$. Therefore, if the material did originate in an AGB star, it must have been added to the surface of these stars through binary mass transfer.

A mass-transfer scenario would imply the current Group 3 CDGs should be in binary systems. We checked for binarity in the literature, consulting multiple catalogs (Mason et al. 2001; Dommanget & Nys 2002; Kovaleva et al. 2015; El-Badry et al. 2021), and found 12 giants either in multiple systems or in a binary system. This is 41% of the 29 known CDGs, which is broadly consistent with the expected binary fraction in this mass range ($\sim 48\%$; Parker & Meyer 2014). Thus, there appears to be no bias toward a high binary fraction that would be expected from this scenario. We note however that this result may be affected by incomplete data. A dedicated binary survey of these stars would be needed to be certain of the true binary fraction. If the AGB binary mass-transfer scenario were correct, we would also expect the primary (donor) stars to have evolved to the WD by now, so we would expect to see Group 3 stars with WD companions. We only find three of the 29 Group 3 stars with evolutionary phase identifications in the literature. All of these are identified as MS–MS binaries (El-Badry et al. 2021), at odds with the scenario. More data on binarity is required to properly test the AGB binary mass-transfer theory.

4.5. Possible Explanations for the Origin of Group 1 CDG Stars Based on Our New Findings

4.5.1. Normal-luminosity-RC CDG Stars (Group 1): Core-flash Mixing?

Our sample of normal-luminosity-RC CDG stars (Group 1 in Table 4) has luminosities consistent with the background sample of RC stars (hence the name; Figure 10). They also mostly have normal RC radii, although there is one outlier that has a large radius. They have less extreme chemical patterns, being less C-deficient and less N-enhanced. A striking difference with the overluminous sample is that they do not

have any Na overabundance—they all have scaled-solar Na. This suggests the burning that led to the chemical pattern of these stars was not at such high temperature, with just the CN cycle operating ($\approx 20\text{--}40$ MK; Adamczak & Lambert 2013). The masses of the normal-luminosity-RC CDGs are similar to the overluminous sample but biased to slightly lower masses (Figure 4; Table 4). Despite this, the sample is also missing the lowest-mass stars as compared to the background RC sample, with no stars of mass less than $1.2 M_{\odot}$. This could be evidence of a merger scenario, discussed in Section 4.5.2. With respect to seismology, they primarily follow the normal RC distribution (see seismic diagram in Figure 10). Interestingly, most of this group is very Li-rich. Six out of the seven stars ($\approx 86\%$) for which we have spectra are Li-rich (Table 3). We discuss the remarkable number of Li-rich CDGs in Section 4.6.

The fact that CDGs are generally not found at luminosities below the RC is suggestive of a pollution event near the RGB tip. Given the mass range of our Group 1 stars (Table 4), they should all have gone through degenerate ignition of He in the core—the core He flash (CHeF). Although envelope pollution has been suggested at the CHeF (e.g., Deupree & Wallace 1987; Izzard et al. 2007; Mocák et al. 2009), it is expected that any mixing at the core helium flash would result in an *increase* in carbon at the surface (e.g., Deupree & Wallace 1987; Izzard et al. 2007; Mocák et al. 2009), incompatible with the C-deficient stars. However a “weaker” pollution event has been suggested at the CHeF to explain Li-rich giants (Kumar et al. 2011), which are primarily RC stars too, and also to explain “Li-enhanced” RC stars (Kumar et al. 2020; Schwab 2020). One might imagine a flash-induced mixing scenario between these two extremes, whereby CN(O) burning operates, producing N-enhancement and C-deficiency. As mentioned, the fact that there is no Na enhancement in these stars means that the hypothesized extra mixing would not have to reach very high burning temperatures. As far as we are aware, CHeF extra-mixing in this regime has not yet been investigated. Finally, since there are so few CDGs (0.15% of our sample; Section 2), this proposed extra-mixing event would only occur in a very small fraction of stars.

4.5.2. Normal-luminosity-RC CDG Stars (Group 1): Mergers?

As mentioned above, the normal-luminosity RC CDGs are low mass but show a bias against the lowest-masses relative to the background RC sample (Figure 10). This is similar to our overluminous sample (Group 2 in Table 4), for which we concluded the merger scenario to be the most likely. In particular, for the normal-luminosity sample, there are no stars below $\approx 1.2 M_{\odot}$, and the average mass of the stars is $1.5 M_{\odot}$. This could be the signature of a merger-product population since mergers tend to produce more-massive stars.

Moreover, in the seismic diagram (Figure 10(c)), although on the whole, this sample overlaps the background RC sample, it does show significant dispersion. Half of the sample (four out of eight stars) is on the extremes of the background distribution. Further, two of them clearly fall above the general trend (having relatively high $\nu_{\max}^{0.75} / \Delta\nu$ and ν_{\max}), near the position of the overluminous-RC CDGs. This is further suggestive of the merger scenario, and the dispersion may be related to variation in the progenitors. We note that these stars do not appear to be stripped stars as identified by Li et al. (2022; orange symbols in Figure 10).

We suggest that the fact that these stars are not overluminous does not necessarily rule out the merger scenario. This is because there may be a bifurcation in core-mass post merger; lower-mass mergers will undergo the CHeF, whereas higher-mass mergers may not (depending on the resultant merged core mass). Alternatively, other merger scenarios or physics (e.g., Zhang & Jeffery 2013) could produce the variation.

As mentioned, the chemical signature of these normal-luminosity RC CDGs is relatively limited, compared to the overluminous sample. This could be consistent with the lower masses of the normal-luminosity stars (on average $0.3 M_{\odot}$ lower), such that lower-mass mergers are likely to result in lower-temperature burning, which would give less extreme chemical patterns.

4.6. Link to the Li-rich Giants

Considering the rarity of Li-rich giants ($\approx 3\%$ on the RC; Kumar et al. 2020), there are a remarkable number of Li-rich C-deficient stars. In our sample for which we have spectra, 50% (6/12 stars) have $A(\text{Li}) > 1.8$ dex (1.8 dex is our detection limit; Section 3.5.3). In our overluminous literature sample with spectroscopic data (black open squares in Figure 10), about 80% (five out of six stars) are Li-rich (also see Table 4).

We compiled a comprehensive literature sample of previously known CDGs for which Li abundances are available (Adamczak & Lambert 2013; Palacios et al. 2016) and found that $\sim 50\%$ of those stars (14/29 stars) are Li-rich ($A(\text{Li}) > 1.5$ dex). Clearly there is an extremely strong bias toward CDGs also being Li-rich giants. This suggests that they may be related in some way, so formation scenarios for the CDGs may also apply to the Li-rich giant population (and vice versa).

As discussed above, we have two main theories for our CDGs: CHeF-mixing and low-mass stellar mergers. For our overluminous-RC CDGs we believe the merger scenario is the most likely, and for the normal-luminosity-RC CDGs, we cannot differentiate between the CHeF-mixing and merger scenarios.

Li-rich giants are generally (normal-luminosity) RC stars (Kumar et al. 2011; Figure 9 of Zhang et al. 2020; Singh et al. 2021). That both Li-rich giants and CDGs are primarily RC stars is another striking parallel between these two chemically peculiar populations, only just revealed by the current study.

As we suggested in Section 4.5.1 for our CDGs, it has also been suggested that CHeF-mixing may be responsible for the Li enrichment in Li-rich giants (Kumar et al. 2011, 2020; Schwab 2020).

The merger scenario has also been suggested for Li-rich giants by Zhang et al. (2020) who provided population synthesis models. Yan et al. (2021) further investigated this merger scenario. They were able to explain most features of the Li-rich giants; however, they could not explain the nitrogen enhancements in many of the stars (see their Figure 2). Nitrogen enhancement implies that the material has experienced CN(O) burning, so we would expect C to have been depleted in some of the Li-rich giants, particularly the most N-rich stars. To check this, in Figure 13 we compare the C and N abundances (and masses) for a sample of Li-rich giants to various samples of CDGs. Indeed, taking Li-rich giants with strong N-enhancement ($[\text{N}/\text{Fe}] > +0.4$ dex), we find $\sim 85\%$ of them to be CDGs as per our definition given in Section 2.2 ($[\text{C}/\text{Fe}] < -0.4$ dex). In fact, six of our CDGs are included in

the Li-rich study of Yan et al. (2021). This again shows the significant overlap in Li-rich and CDGs, which can be seen visually in Figure 13.

Li-rich giants have low $^{12}\text{C}/^{13}\text{C}$ ratios, being mostly in the range of 5–10 (although in some cases it is close to 30; Kumar et al. 2011). This compares well with the CDGs for which $^{12}\text{C}/^{13}\text{C}$ has been measured, which also show low values (Table 4). As mentioned above, we do not have $^{12}\text{C}/^{13}\text{C}$ for our Group 1 and Group 2 stars, but their very low [C/N] indicates they have also undergone significant burning, albeit not to equilibrium (Section 4.2.2). Thus, it is expected that their $^{12}\text{C}/^{13}\text{C}$ must be fairly low.¹⁴

Given the aforementioned similarities/overlap between Li-rich giants and the CDGs, we speculate that we are seeing a spectrum of merger products, varying in progenitor mass. In Table 4 we see that Li-rich giants appear in Groups 1 and 3, which we have identified as having distinct chemical enrichments in CNO and Na. This shows that Li is not the best tracer for identifying chemically peculiar stars. This is likely due to its easily produced and easily destroyed nature. We note that the majority of Li-rich giants do not show signs of CNO burning in their envelopes (Figure 13). If we extend the merger hypothesis to these stars, it may indicate lower-temperature burning and therefore lower-mass progenitors. Alternatively, their Li may have been formed at the core helium flash (Kumar et al. 2020; Schwab 2020).

4.7. Globular Cluster Link

As noted by Zhang & Jeffery (2013), the chemical pattern of their B2 merger model is similar to the abundance anomaly patterns found in second-generation globular cluster populations: low C, high N, and enhanced Na. We also identified the B2 model as a possible match for many of our CDGs, since this pattern also qualitatively matches them. However, as with the Zhang & Jeffery (2013) model, the CDGs do not match the oxygen depletion seen in GCs (Gratton et al. 2000), which gives rise to the Na–O anticorrelation. As speculated by Zhang & Jeffery (2013), this may be a metallicity effect—metal-poor CDGs (or merger models) may deplete O. This is an enticing scenario for GCs since it is expected that stellar interactions are relatively common in such dense stellar environments, with mergers being a key binary destruction pathway (see, e.g., Figure 4 in Ivanova et al. 2005).

5. Conclusion

In this study, we addressed the long-standing questions related to the mass and evolutionary phase of the CDGs with the help of asteroseismology (Kepler and TESS missions), spectroscopy (APOGEE and LAMOST surveys), and astrometry (Gaia). We list our wide-ranging results in Section 4.1 (also see Table 4). We briefly summarize the most important points here.

We found 15 newly identified CDGs in the Kepler field. As a fraction of our Kepler-APOGEE sample, CDGs represent only 0.15% of the stars and hence are very rare.

For the first time, we unambiguously identified the evolutionary state of CDGs. Remarkably, we found 93% of our sample to be in the RC core He-burning phase. This places strong constraints on formation scenarios. The lack of MS,

SGB, and RGB carbon-deficient stars rules out theories that posit the chemical pollution occurred early in CDG evolution, be it through self-pollution or external pollution scenarios.

In contrast to previous literature, where wGb stars were considered to be of intermediate mass ($M \approx 2.5 M_{\odot} - 5.0 M_{\odot}$) based on their position on the HRD, the Kepler-based asteroseismic masses reveal that our sample of CDGs comprises primarily low-mass stars ($M \lesssim 2 M_{\odot}$). We also determined asteroseismic masses for a small sample of previously known wGb stars, finding that their seismic masses are also primarily low. This finding places further constraints on any formation scenario.

We find definite demarcations in the chemical patterns of CDGs, which enabled us to split them into three groups, in increasing order of degree of pollution. The first, Group 1, is characterized by nonequilibrium CN-cycle burning pattern, while Group 2 is similar but slightly more extreme, but with an additional enhancement of Na. Group 3 has an even more extreme chemical pattern and is distinct in that its pattern shows dredge-up of He-burning products has occurred, with strong hydrogen burning on top of this. The chemical patterns through the three groups also suggest an increasing temperature of hydrogen burning.

We find a bimodality (roughly 60:40) in luminosity within our sample, with one group (Group 1) having normal RC luminosity and the other group (Group 2) being about a factor of 2 more luminous than expected for their masses ($\approx 60 L_{\odot}$ versus $120 L_{\odot}$). We concluded that stars in the more luminous group are likely merger products, having formed through the merger of a HeWD and an RGB star. One of the low-mass merger models of Zhang & Jeffery (2013) is a good qualitative match for these stars. Previously known wGb stars for which we have TESS seismology are also overluminous, and we suggest they were formed through mergers as well. They do have more extreme chemical patterns and, importantly, are enriched in CNO elements, most likely from the dredge-up of He-burning products. In the merger scenario, this suggests that the progenitor stars would have been more massive, leading to more extreme mixing and burning (Zhang et al. 2020).

For the normal-luminosity-RC CDGs (Group 1), we cannot distinguish between the two remaining formation scenarios. The first is a possible pollution event near the end of the RGB, likely at the core He-flash. This has also been suggested for the Li-rich giants (Kumar et al. 2011, 2020; Schwab 2020; Singh et al. 2021). Interestingly, about 90% of our normal-luminosity-RC CDGs are also Li-rich giants. The second suggested scenario is that these stars are low-mass merger products like the overluminous groups, just with less extreme chemical pollution, which might indicate less-massive progenitor masses.

A significant fraction of our CDGs (50%) are also Li-rich giants. This is 17 times higher than the expected fraction of 3%. Thus, there is a strong overlap between CDGs and Li-rich giants. That said, there is variation between our three proposed CDG groups—one group is 90% Li-rich, the second has zero Li-rich members, and the third group is 50% Li-rich (85% in our small TESS sample, which is biased to lower luminosities). As is well recognized, lithium is a special element—it is easily produced but also easily destroyed. Thus, it is not surprising to see this variation. In the merger models of Zhang & Jeffery (2013) and Zhang et al. (2020), they also found Li to

¹⁴ Also see the C-poor Li-rich giant in Silva Aguirre et al. (2014), which has an upper limit for $^{12}\text{C}/^{13}\text{C}$ of 20.

sometimes be produced and sometimes to be produced then destroyed.

To summarize, based on our new data on CDGs, we suggest the following scenarios for their formation, for the three groups we have defined:

1. Group 1 (normal-luminosity-RC CDGs): Core He-flash pollution event, or low-mass mergers between HeWDs and RGB stars.
2. Group 2 (overluminous-RC CDGs): Higher-mass mergers between HeWDs and RGB stars.
3. Group 3 (previously known wGb stars, many overluminous): Mergers between HeWDs and RGB stars, or binary mass-transfer from intermediate-mass AGB stars.

As can be seen, stellar mergers feature as a possibility across all groups. It is tempting to see the different groups of CDGs as being produced by mergers with different progenitor masses. More observations are required to confirm (or disprove) these proposed scenarios.

Acknowledgments

This study is supported by the National Natural Science Foundation of China under grant Nos. 11988101, 11890694, and 11873052 and National Key R&D Program of China No. 2019YFA0405500. S.M. acknowledges the support by CAS-TWAS Presidents fellowship for International Doctoral Students. S.M. thanks Raghubar Singh for helpful conversations. We thank Evgenii Neumerzhitskii for the use of his plotting routine. Funding for LAMOST (www.lamost.org) has been provided by the Chinese NDRC. LAMOST is operated and managed by the National Astronomical Observatories, CAS. This work has made use of data from the European Space Agency (ESA) mission Gaia (<https://www.cosmos.esa.int/gaia>). We made use of the SIMBAD database and the Vizier catalog access tool, CDS, Strasbourg, France. S.W.C. acknowledges federal funding from the Australian Research Council through a Future Fellowship (FT160100046) and Discovery Projects (DP190102431 & DP210101299). Parts of this research was supported by the Australian Research Council Centre of Excellence for All Sky Astrophysics in 3 Dimensions (ASTRO 3D), through project No. CE170100013. This research was supported by use of the Nectar Research Cloud, a collaborative Australian research platform supported by the National Collaborative Research Infrastructure Strategy (NCRIS). S.W.C. thanks Carolyn Doherty for interesting and helpful discussions.

ORCID iDs

Sunayana Maben  <https://orcid.org/0000-0001-9974-1754>

Gang Zhao  <https://orcid.org/0000-0002-8980-945X>

References

- Abdurro'uf, Accetta, K., Aerts, C., et al. 2022, *ApJS*, 259, 35
- Adameczak, J., & Lambert, D. L. 2013, *ApJ*, 765, 155
- Alonso, A., Arribas, S., & Martínez-Roger, C. 1999, *A&AS*, 140, 261
- Arnould, M., Goriely, S., & Jorissen, A. 1999, *A&A*, 347, 572
- Astropy Collaboration, Price-Whelan, A. M., Sipőcz, B. M., et al. 2018, *AJ*, 156, 123
- Astropy Collaboration, Robitaille, T. P., Tollerud, E. J., et al. 2013, *A&A*, 558, A33
- Bailer-Jones, C. A. L., Rybizki, J., Fouesneau, M., Demleitner, M., & Andrae, R. 2021, *yCat*, I/352
- Bedding, T. R., Mosser, B., Huber, D., et al. 2011, *Natur*, 471, 608
- Bidelman, W. P. 1951, *ApJ*, 113, 304
- Bidelman, W. P., & MacConnell, D. J. 1973, *AJ*, 78, 687
- Bildsten, L., Paxton, B., Moore, K., & Macias, P. J. 2012, *ApJL*, 744, L6
- Blanco-Cuaresma, S. 2019, *MNRAS*, 486, 2075
- Blanco-Cuaresma, S., Soubiran, C., Heiter, U., et al. 2014, *A&A*, 569, A111
- Bland-Hawthorn, J., & Gerhard, O. 2016, *ARA&A*, 54, 529
- Bond, H. E. 2019, *ApJ*, 887, 12
- Borucki, W. J., Koch, D., Basri, G., et al. 2010, *Sci*, 327, 977
- Brown, T. M., Gilliland, R. L., Noyes, R. W., & Ramsey, L. W. 1991, *ApJ*, 368, 599
- Campbell, S. W., & Lattanzio, J. C. 2008, *A&A*, 490, 769
- Castelli, F., & Kurucz, R. L. 2003, in *IAU Symp. 210, Modelling of Stellar Atmospheres*, ed. N. Piskunov, W. W. Weiss, & D. F. Gray (Cambridge: Cambridge Univ. Press), A20
- Caughlan, G. R. 1965, *ApJ*, 141, 688
- Clayton, D. D. 1983, *Principles of Stellar Evolution and Nucleosynthesis* (Chicago, IL: Univ. Chicago Press), 1983
- Constantino, T., Campbell, S. W., & Lattanzio, J. C. 2017, *MNRAS*, 472, 4900
- Cottrell, P. L., & Norris, J. 1978, *ApJ*, 221, 893
- Dearborn, D. S. P., Eggleton, P. P., & Schramm, D. N. 1976, *ApJ*, 203, 455
- Dearborn, D. S. P., Tinsley, B. M., & Schramm, D. N. 1978, *ApJ*, 223, 557
- Deupree, R. G., & Wallace, R. K. 1987, *ApJ*, 317, 724
- Dommanget, J., & Nys, O. 2002, *yCat*, I/274
- El-Badry, K., Rix, H. W., & Heintz, T. M. 2021, *MNRAS*, 506, 2269
- Elsworth, Y., Hekker, S., Basu, S., et al. 2017, *MNRAS*, 466, 3344
- Gaia Collaboration, Prusti, T., de Bruijne, J. H. J., et al. 2016, *A&A*, 595, A1
- Gaia Collaboration, Vallenari, A., Brown, A. G. A., et al. 2023, *A&A*, 674, 22
- García Pérez, A. E., Allende Prieto, C., Holtzman, J. A., et al. 2016, *AJ*, 151, 144
- Gerber, J. M., Briley, M. M., & Smith, G. H. 2019, *AJ*, 157, 154
- Girardi, L. 2016, *ARA&A*, 54, 95
- Gratton, R. G., Sneden, C., Carretta, E., et al. 2000, *A&A*, 354, 169
- Green, G. M., Schlafly, E., Zucker, C., Speagle, J. S., & Finkbeiner, D. 2019, *ApJ*, 887, 93
- Grevesse, N., Asplund, M., & Sauval, A. J. 2007, *SSRv*, 130, 105
- Herwig, F., Bloeker, T., Schoenberner, D., et al. 1997, *A&A*, 324, L81
- Holtzman, J. A., Hasselquist, S., Shetrone, M., et al. 2018, *AJ*, 156, 125
- Hon, M., Huber, D., Kuzlewicz, J. S., et al. 2021, *ApJ*, 919, 131
- Howell, M., Campbell, S. W., Stello, D., et al. 2022, *MNRAS*, 515, 3184
- Huber, D., Bedding, T. R., Stello, D., et al. 2011, *ApJ*, 743, 143
- Iben, I., & Renzini, A. 1984, *PhR*, 105, 329
- Iben, I. 1964, *ApJ*, 140, 1631
- Iben, I. J. 1967, *ApJ*, 147, 624
- Ivanova, N., Belczynski, K., Fregeau, J. M., et al. 2005, *MNRAS*, 358, 572
- Izzard, R. G., Jeffery, C. S., & Lattanzio, J. 2007, *A&A*, 470, 661
- Johnson, D. R. H., & Soderblom, D. R. 1987, *AJ*, 93, 864
- Jönsson, H., Holtzman, J. A., Allende Prieto, C., et al. 2020, *AJ*, 160, 120
- Jurić, M., & Ivezić, Ž. 2008, *ApJ*, 673, 864
- Karakas, A. I. 2003, PhD thesis, Monash Univ. Australia
- Karakas, A. I., & Lattanzio, J. C. 2014, *PASA*, 31, e030
- Kjaergaard, P., Gustafsson, B., Walker, G. A. H., & Hultqvist, L. 1982, *A&A*, 115, 145
- Kjeldsen, H., & Bedding, T. R. 1995, *A&A*, 293, 87
- Kovaleva, D., Kaygorodov, P., Malkov, O., Debray, B., & Oblak, E. 2015, *A&C*, 11, 119
- Kumar, Y. B., Reddy, B. E., Campbell, S. W., et al. 2020, *NatAs*, 4, 1059
- Kumar, Y. B., Reddy, B. E., & Lambert, D. L. 2011, *ApJL*, 730, L12
- Lambert, D. L., & Ries, L. M. 1977, *ApJ*, 217, 508
- Li, Y., Bedding, T. R., Li, T., et al. 2020, *MNRAS*, 495, 2363
- Li, Y., Bedding, T. R., Murphy, S. J., et al. 2022, *NatAs*, 6, 673
- Lind, K., Asplund, M., & Barklem, P. S. 2009, *A&A*, 503, 541
- Maben, S., Kumar, Y., Reddy, B. E., Campbell, S. W., & Zhao, G. 2023, *MNRAS*, 525, 4554
- Majewski, S. R., Schiavon, R. P., Frinchaboy, P. M., et al. 2017, *AJ*, 154, 94
- Martell, S. L., Smith, G. H., & Briley, M. M. 2008, *AJ*, 136, 2522
- Mason, B. D., Wycoff, G. L., Hartkopf, W. I., Douglass, G. G., & Worley, C. E. 2001, *AJ*, 122, 3466
- Mathur, S., Huber, D., Batalha, N. M., et al. 2017, *ApJS*, 229, 30
- Miglio, A. 2012, in *Red Giants as Probes of the Structure and Evolution of the Milky Way*, ed. A. Miglio, J. Montalbán, & A. Noels (Berlin: Springer), 11
- Miglio, A., Chaplin, W. J., Brogaard, K., et al. 2016, *MNRAS*, 461, 760
- Mishenina, T. V., Bienaymé, O., Garbaneva, T. I., et al. 2006, *A&A*, 456, 1109
- Mocák, M., Müller, E., Weiss, A., et al. 2009, *A&A*, 501, 659
- Morel, T., Miglio, A., Lagarde, N., et al. 2014, *A&A*, 564, A119
- Mosser, B., Benomar, O., Belkacem, K., et al. 2014, *A&A*, 572, L5
- Nissen, P. E. 2004, in *Origin and Evolution of the Elements*, ed. A. McWilliam & M. Rauch (Cambridge: Cambridge Univ. Press), 154

- Palacios, A., Jasniewicz, G., Masseron, T., et al. 2016, *A&A*, **587**, A42
- Palacios, A., Parthasarathy, M., Bharat Kumar, Y., & Jasniewicz, G. 2012, *A&A*, **538**, A68
- Parker, R. J., & Meyer, M. R. 2014, *MNRAS*, **442**, 3722
- Parthasarathy, M., & Rao, N. K. 1980, *Ap&SS*, **73**, 251
- Paxton, B., Bildsten, L., Dotter, A., et al. 2011, *ApJS*, **192**, 3
- Paxton, B., Smolec, R., Schwab, J., et al. 2019, *ApJS*, **243**, 10
- Pinsonneault, M. H., Elsworth, Y. P., Tayar, J., et al. 2018, *ApJS*, **239**, 32
- Placco, V. M., Sneden, C., Roederer, I. U., et al. 2021, *RNAAS*, **5**, 92
- Postnov, K. A., & Yungelson, L. R. 2014, *LRR*, **17**, 3
- Reimers, D. 1975, *MSRSL*, **8**, 369
- Riello, M., De Angeli, F., Evans, D. W., et al. 2021, *A&A*, **649**, A3
- Romano, D., Matteucci, F., Zhang, Z. Y., et al. 2019, *MNRAS*, **490**, 2838
- Schwab, J. 2020, *ApJL*, **901**, L18
- Serenelli, A., Johnson, J., Huber, D., et al. 2017, *ApJS*, **233**, 23
- Sharma, S., Stello, D., Bland-Hawthorn, J., Huber, D., & Bedding, T. R. 2016, *ApJ*, **822**, 15
- Shetrone, M., Tayar, J., Johnson, J. A., et al. 2019, *ApJ*, **872**, 137
- Shetrone, M. D., Sneden, C., & Pilachowski, C. A. 1993, *PASP*, **105**, 337
- Silva Aguirre, V., Ruchti, G. R., Hekker, S., et al. 2014, *ApJL*, **784**, L16
- Singh, R., Reddy, B. E., Campbell, S. W., Kumar, Y. B., & Vrad, M. 2021, *ApJL*, **913**, L4
- Snedden, C., Lambert, D. L., Tomkin, J., & Peterson, R. C. 1978, *ApJ*, **222**, 585
- Snedden, C. A. 1973, PhD thesis, Univ. Texas, Austin
- Stello, D., Huber, D., Bedding, T. R., et al. 2013, *ApJL*, **765**, L41
- Stetson, P. B. 2000, *PASP*, **112**, 925
- Tautvaišienė, G., Edvardsson, B., Puzeras, E., et al. 2010, *MNRAS*, **409**, 1213
- Ting, Y. S., Hawkins, K., & Rix, H. W. 2018, *ApJL*, **858**, L7
- Tomkin, J., Woolf, V. M., Lambert, D. L., & Lemke, M. 1995, *AJ*, **109**, 2204
- Ulrich, R. K. 1986, *ApJL*, **306**, L37
- Venn, K. A., Irwin, M., Shetrone, M. D., et al. 2004, *AJ*, **128**, 1177
- Vrad, M., Mosser, B., & Samadi, R. 2016, *A&A*, **588**, A87
- White, T. R., Bedding, T. R., Stello, D., et al. 2011, *ApJ*, **743**, 161
- Yan, H. L., Zhou, Y. T., Zhang, X., et al. 2021, *NatAs*, **5**, 86
- Yu, J., Huber, D., Bedding, T. R., et al. 2018, *ApJS*, **236**, 42
- Zhang, X., & Jeffery, C. S. 2013, *MNRAS*, **430**, 2113
- Zhang, X., Jeffery, C. S., Li, Y., et al. 2020, *ApJ*, **889**, 33
- Zhao, G., Chen, Y. Q., Shi, J. R., et al. 2006, *ChJAA*, **6**, 265
- Zhao, G., Zhao, Y. H., Chu, Y. Q., Jing, Y. P., & Deng, L. C. 2012, *RAA*, **12**, 723